Proposal to PAC48

Beam Charge Asymmetries for Deeply Virtual Compton Scattering on the Proton at CLAS12

M. Battaglieri, V. Burkert[⋆†], A. Deur, L. Elouadrhiri[⋆], J. Grames, D. Higinbotham, V. Kubarovsky, M. McCaughan, E. Pasyuk, M. Poelker

Thomas Jefferson National Accelerator Facility
12000 Jefferson Avenue, Newport News, VA 23606, USA

M. Caudron, L. Causse, P. Chatagnon, R. Dupré, M. Ehrhart, S. Habet, A. Hobart, D. Marchand, C. Muñoz Camacho, S. Niccolai[⋆], H.-S. Ko, K. Price, V. Sergeyeva, E. Voutier[⋆†], S. Zhao

Laboratoire de Physique des 2 Infinis Irène Joliot-Curie
Université Paris-Saclay, CNRS/IN2P3, IJCLab
15 rue Georges Clémenceau, 91405 Orsay cedex, France

R. Capobianco[1], S. Diehl[1,2], F.-X. Girod[1,⋆], K. Joo[1], A. Kim[1], V. Klimenko[1], R. Santos[1], P. Stoler[1]

[1] *University of Connecticut, Department of Physics*
2152 Hillside Road, Storrs, CT U-3046, USA

[2] *Universität Gießen*
Luwigstraße 23, 35390 Gießen, Deutschland

B. Raue

Florida International University
Modesto A. Maidique Campus
11200 SW 8th Street, CP 204, Miami, FL 33199, USA

[⋆] *Spokesperson*
[†] *Contact person*

P.L. Cole

Lamar University, Physics Department
4400 MLK Boulevard, Beaumont, TX 77710, USA

A. Bianconi, G. Costantini, M. Leali, V. Mascagna, L. Venturelli

Università degli Studi di Brescia
Via Branze, 38 - 25121 Brescia, Italia

Istituto Nazionale di Fisica Nucleare
Sezione di Pavia
Via Agostino Bassi, 6 - 27100 Pavia, Italia

Z. Zhao

Duke University
120 Science Drive, Durham, NC 27708, USA

P. Gueye

Michigan State University
640 South Shaw Lane, East Lansing, MI 48824, USA

L. Barion[3], G. Ciullo[3,4], M. Contalbrigo[3], P. Lenisa[3,4],
A. Movsisyan[3], L. Pappalardo[3,4]

[3]*Istituto Nazionale di Fisica Nucleare*
Sezione di Ferrara
Via Saragat, 1 - 44122 Ferrara, Italia

[4]*Università di Ferrara*
Via Ludovico Ariosto, 35 - 44121 Ferrara, Italia

M. Defurne

Institut de Recherche sur les Lois Fondamentales de l'Univers
Commissariat à l'Energie Atomique, Université Paris-Saclay
91191 Gif-sur-Yvette, France

B. McKinnon

University of Glasgow
University Avenue, Glasgow G12 8QQ, United Kingdom

I. Fernando

Hampton University, Physics Department
100 E Queen Street, Hampton, VA 23668, USA

T. Chetry

Mississippi State University
355 Lee Boulevard, Mississippi State, MS 39762, USA

C.E. Hyde

Old Dominion University
5115 Hampton Boulevard, Norfolk, VA 23529, USA

T. Forest

Idaho State University
921 South 8th Avenue, Pocatello, ID 83209, USA

J.C. Bernauer

Stony Brook University
100 Nicolls Road, Stony Brook, NY 11794, USA

A. Filippi

Istituto Nazionale di Fisica Nucleare
Sezione di Torino
Via P. Giuria, 1 - 10125 Torino, Italia

A. Afanasev, I. Strakovsky

The George Washington University
221 I Street NW, Washington, DC 20052, USA

and the CLAS Collaboration

22 June 2020

Abstract

The parameterization of the nucleon structure through Generalized Parton Distributions (GPDs) shed a new light on the nucleon internal dynamics. For instance, GPDs provide an unprecedented experimental access to the orbital momentum of the nucleon and the distribution of forces experienced by partons. For its direct interpretation, Deeply Virtual Compton Scattering (DVCS) is the golden channel for GPDs investigation. The DVCS process interferes with the Bethe-Heitler (BH) mechanism to constitute the leading order amplitude of the $eN \to eN\gamma$ process. The study of the $ep\gamma$ reaction with polarized positron and electron beams gives a complete set of unique observables to unravel the different contributions to the $ep\gamma$ cross section. This separates the different reaction amplitudes, providing a direct access to their real and imaginary parts, which greatly simplifies physics interpretation. This procures crucial constraints on the model dependences and associated systematic uncertainties on GPDs extraction. The real part of the BH-DVCS inteference amplitude is particularly sensitive to the D-term which parameterizes the Gravitational Form Factors of the nucleon. The separation of the imaginary parts of the interference and DVCS amplitudes provides insights on possible higher twist effects.

The ability of the CEBAF injector for the efficient production of polarized positrons was recently demonstrated. The Polarized Electrons for Polarized Positrons (PEPPo) technique offers a direct and accessible method for polarized positrons production, particularly suitable for creating such beams at JLab. The implementation of PEPPo at CEBAF is evaluated to produce at least 100 nA 60% polarized and 5 μA unpolarized positron beams.

We propose to measure the unpolarized and polarized Beam Charge Asymmetries (BCAs) of the $\vec{e}^{\pm}p \to e^{\pm}p\gamma$ process on unpolarized Hydrogen with `CLAS12`, using polarized positron and electron beams at 10.6 GeV. The azimuthal and t-dependences of the unpolarized and polarized BCAs will be measured over a large (x_B, Q^2) phase space using a 2400 hours run with a luminosity of $0.6{\times}10^{35}$ cm$^{-2}{\cdot}$s^{-1}.

Preample

$\sim . \sim . \sim$

The Jefferson Laboratory has been a world center for the exploration of the internal structure and dynamics of nucleons and nuclei for over 25 years: first with the 6 GeV energy reach of the original CEBAF, and for the past several years with the energy-upgraded 12 GeV electron accelerator and the new and upgraded equipment in the experimental end stations. Nearly all experiments have been carried out with the extremely precise electron beam of CEBAF delivered concurrently to the three and now four experimental end stations. Some of the high impact science topics can be most cleanly explored in comparison of measurements carried out with electrons and with positrons. The recent development and successful test of a spin polarized positron source at Jefferson Lab has opened up a new line of measurements that could complement the electron-induced measurements and lead to new insights into the structure of matter.

We propose to carry out Deeply Virtual Compton Scattering (DVCS) measurements separately with electron and positron beams. In the DVCS process the final state real photon is emitted by the active parton. The DVCS process is experimentally indistinguishable from the Bethe-Heitler (BH) process, for which the electron/positron radiates a hard real photon either before or after the interaction vertex. The BH and DVCS interfere at the amplitude level. The total cross section for the deep lepto-production of a real photon includes the BH amplitude squared, the DVCS amplitude squared, and the interference term.

The comparison of DVCS measurements with electrons $e^-(p, e^- p\gamma)$ and with positrons $e^+(p, e^- p\gamma)$ isolates the interference term, which is directly related to the real part of a complex Compton Form Factor (CFF). As such they provide the cleanest, model-independent access to this crucial observable, without the need for additional theoretical assumptions in the extraction procedure. The imaginary part can be directly accessed in the beam spin asymmetry employing the highly polarized electron or positron beam.

Full knowledge of the real and imaginary parts of the CFF enables employing a dispersion relation that allows to determine a new form factor which is at the base of a new line of research to access the mechanical or gravitational properties of the nucleon. These particle properties can be directly measured only in the interaction of gravity with matter, which is experimentally a highly impractical proposition. The investigation of these properties in the valence region accessible at CEBAF energies would procure the basis for an extension of this project into the sea-quarks and gluonic sectors at the Electron Ion Collider.

Table of contents

1 Introduction

The challenge of the understanding of the structure and dynamics of the nucleon remains a major goal of modern Nuclear Physics despite extensive experimental scrutiny. From the initial measurements of elastic electromagnetic form factors to the accurate determination of parton distributions through deep inelastic scattering, the experiments have increased in statistical and systematic precision thanks to the development of performant electron beams together with capable detector systems. The availability of high intensity continuous polarized electron beams with high energy is providing today an unprecedented but still limited insight into the nucleon structure problem.

Over the past two decades, the Generalized Parton Distribution (GPD) paradigm [Mul94] offered a universal and most powerful way to characterize the nucleon structure, generalizing and unifying the special cases of form factors and parton distribution functions (see [Die03, Bel05] for a review). The GPDs are the Wigner quantum phase space distribution of partons in the nucleon, describing the simultaneous distribution of particles with respect to both the position and momentum in a quantum-mechanical system [Ji03, Bel04]. They encode the correlation between partons and consequently reveal not only the spatial and momentum densities, but also the correlation bewteen the spatial and momentum distributions, *i.e.* how the spatial shape of the nucleon changes when probing partons of different momentum fraction x of the nucleon. The combination of longitudinal and transverse degrees of freedom is responsible for the richness of this framework. The second moment in x of GPDs are related to form factors that allow us to quantify how the orbital motion of partons in the nucleon contributes to the nucleon spin [Ji97], and how the parton masses and the forces on partons are distributed in the transverse space [Pol03], a question of crucial importance for the understanding of the dynamics underlying nucleon structure, and which may provide insight into the dynamics of confinement.

The mapping of the nucleon GPDs, and the detailed understanding of the spatial quark and gluon structure of the nucleon, have been widely recognized as key objectives of Nuclear Physics of the next decades. This requires a comprehensive program, combining results of measurements of a variety of processes in eN scattering with structural information obtained from theoretical studies, as well as expected results from future lattice QCD calculations. Particularly, GPDs can be accessed in the lepto-production of real photons $lN \rightarrow lN\gamma$ through the Deeply Virtual Compton Scattering (DVCS) corresponding to the scattering of a virtual photon into a real photon after interacting with a parton of the nucleon. At leading twist-2, DVCS accesses the 4 quark-helicity conserving GPDs $\{H_q, E_q, \widetilde{H}_q, \widetilde{E}_q\}$ defined for each quark-flavor $q \equiv \{u, d, s...\}$. They enter the cross section with combinations depending on the polarization states of the lepton beam and of the nucleon target, and are extracted from the modulation of experimental observables in terms of the ϕ out-of-plane angle between the leptonic and hadronic planes. This nuclear process of interest interferes with the QED (Quantum ElectroDynamics) radiation of real photons by the incoming and outgoing leptons. The non-ambiguous extraction of GPDs from experimental data not only requires a large set of observables

but also the separation of the different reaction amplitudes contributing to the $lN\gamma$ reaction. The combination of measurements with lepton beams of opposite polarities is an indisputable path towards such separation [Die09].

The production of high-quality polarized positron beams is a highly difficult task that, until recently, was feasible only at large scale accelerator facilities. Relying on the most recent advances in high polarization and high intensity electron sources [Add10], the PEPPo (Polarized Electrons for Polarized Positrons) technique [Abb16], demonstrated at the injector of the Continuous Electron Beam Accelerator Facility (CEBAF), provides a novel and widely accessible approach based on the production, within a tungsten target, of polarized e^+e^- pairs from the circularly polarized bremsstrahlung radiation of a low energy highly polarized electron beam. As opposed to other schemes operating at GeV lepton beam energies [Sok64, Omo06, Ale08], the operation of the PEPPo technique requires only energies above the pair-production threshold and is therefore ideally suited for a polarized positron beam at CEBAF.

This proposal follows the previous Letter-of-Intent LOI12-18-004 [Gra18] where the perspectives of a physics program with positron beams at the Jefferson Lab (JLab) were presented, which encompasses interference physics (GPDs, multi-photon exchange) and tests of the Standard Model (dark photon search). In the line of recommendations of the JLab Program Adivisory Committee [PAC46], we are proposing here to measure the unpolarized and polarized Beam Charge Asymmetries (BCAs) of the lepto-production of real photons on unpolarized Hydrogen with `CLAS12`, using 10.6 GeV polarized positron and electron beams at a luminosity of 0.6×10^{35} cm^{-2}·s^{-1}.

This proposal is organized as follows: in Sec. 2 we review the physics motivations for these measurements and the BCA sensitivity to GPDs in the kinematical domain of interest at `CLAS12`. The impact of positron measurements is addressed in Sec. 3 in terms of the extraction of the physics information. In Sec. 4 we give an overview of the challenges of the production and the operation of polarized positron beams at JLab is then discussed, further supported by two appendices dedicated to changes and technicalities specific of positron beams. In the remaining sections we discuss the experimental configuration of BCA measurements at `CLAS12`, the method for the control of systematic effects attached to the comparison of electron and positron measurements, and the detailed beam time request.

2 Deeply Virtual Compton Scattering

2.1 Separation of reaction amplitudes

Analogously to X-rays crystallography, the virtual light produced by a lepton beam scatters on the partons to reveal the details of the internal structure of the proton. For this direct access to the parton structure, Deeply Virtual Compton Scattering (DVCS) corresponding to the process $\gamma^\star N \to \gamma N$ (Fig. 1)

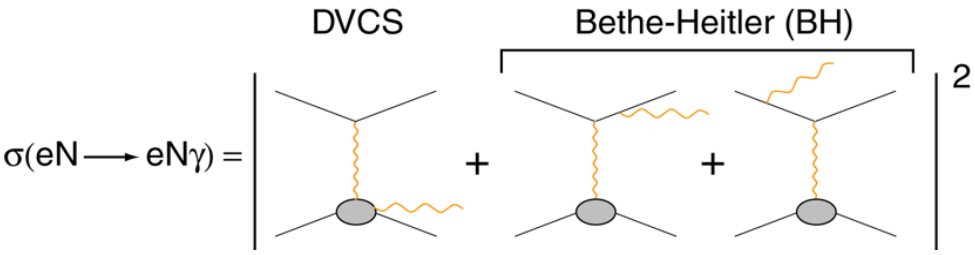

Figure 1. Lowest QED-order amplitude of the electroproduction of real photons off nucleons.

is the golden channel to access GPDs. This process competes with the known BH reaction [Bet34] (Fig. 1) where real photons are emitted from the initial or final leptons. The lepton beam charge (e) and polarization (λ) dependence of the $eN\gamma$ cross section off proton is expressed [Die09]

$$\sigma^e_\lambda = \sigma_{BH} + \sigma_{DVCS} + \lambda\,\widetilde{\sigma}_{DVCS} + e\,(\sigma_{INT} + \lambda\,\widetilde{\sigma}_{INT}) \tag{1}$$

where the index INT denotes the BH-$DVCS$ quantum interference contribution to the cross section; $(\sigma_{BH}, \sigma_{DVCS}, \sigma_{INT})$ represent the beam polarization independent contributions of the cross section, and $(\widetilde{\sigma}_{DVCS}, \widetilde{\sigma}_{INT})$ are the beam polarization dependent contributions [1]. Polarized electron scattering provides the experimental observables

$$\sigma^-_0 = \frac{\sigma^-_+ + \sigma^-_-}{2} = \sigma_{BH} + \sigma_{DVCS} - \sigma_{INT}\,, \tag{2}$$

$$\Delta\sigma^-_\lambda = \frac{\sigma^-_+ - \sigma^-_-}{2} = \lambda\,[\widetilde{\sigma}_{DVCS} - \widetilde{\sigma}_{INT}] \tag{3}$$

involving unseparated combinations of the unknwon INT and $DVCS$ reaction amplitudes. The comparison between polarized electron and polarized positron reactions provides the additional observables

$$\Delta\sigma^C_0 = \frac{\sigma^+_0 - \sigma^-_0}{2} = \sigma_{INT} \tag{4}$$

$$\Delta\sigma^C_\lambda = \frac{\Delta\sigma^+_\lambda - \Delta\sigma^-_\lambda}{2} = \lambda\,\widetilde{\sigma}_{INT} \tag{5}$$

which isolate the interference amplitude. Furthermore,

$$\Sigma\sigma^0_0 = \frac{\sigma^+_0 + \sigma^-_0}{2} = \sigma_{BH} + \sigma_{DVCS} \tag{6}$$

$$\Sigma\sigma^0_\lambda = \frac{\Delta\sigma^+_\lambda + \Delta\sigma^-_\lambda}{2} = \lambda\,\widetilde{\sigma}_{DVCS} \tag{7}$$

[1] $(\sigma_{DVCS}, \sigma_{INT})$ are related further in Sec. 2.3 to the real part of a Compton form factor, while $(\widetilde{\sigma}_{DVCS}, \widetilde{\sigma}_{INT})$ are related to its imaginary part.

which access a pure $DVCS$ signal. Consequently, measuring the lepto-production of real photons off protons with polarized lepton beams of opposite charges allows to separate the four unknown contributions to the $eN\gamma$ cross section.

The essential benefit of polarized positron beams for DVCS is to provide a perfect separation of the reaction amplitudes which consequently permits unambiguous access to GPDs. In absence of such beams, the only possible approach to this separation is to take advantage of the different beam energy sensitivity of the $DVCS$ and INT amplitudes. Recent results [Def17] have shown that this Rosenbluth-like separation cannot be performed without assumptions because of higher twists and higher α_s-order contributions to the cross section. Positron beams offer to this problem an indisputable experimental method.

2.2 Access to Generalized Parton Distributions

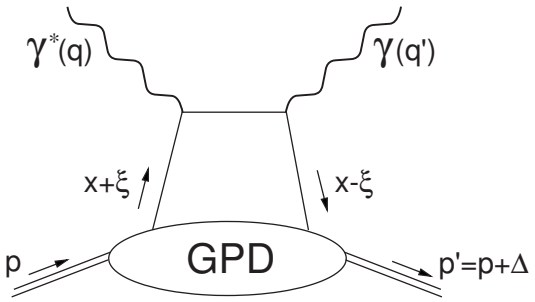

Figure 2. Leading order and leading twist representation of the DVCS reaction amplitude (+ crossed term not shown) with main kinematic parameters of GPDs.

GPDs are universal non-perturbative objects entering the description of hard scattering processes. Although they are not a positive-definite probability density, GPDs correspond to the amplitude for removing a parton carrying some longitudinal momentum fraction x and restoring it with a different longitudinal momentum (Fig. 2). The skewness $\xi \simeq x_B/(2-x_B)$, related to the Bjorken variable $x_B{=}Q^2/2M\omega$, measures the transfer of longitudinal momentum. In this process, the nucleon recieves a four-momentum transfer $t = \boldsymbol{\Delta}^2$ whose transverse component $\boldsymbol{\Delta}_\perp$ is Fourier-conjugate to the transverse distance $\boldsymbol{r}_\perp$ between the active parton and the center-of-mass of spectator partons in the target [Bur07]. In the limit of zero-skewness ($\xi{=}0$), GPDs can be interpreted as the Fourier transform of the distribution in the transverse plane of partons with the longitudinal momentum fraction x [Bur00, Ral02, Die02, Bel02].

GPDs enter the $eN\gamma$ cross section through Compton Form Factors (CFF) $\mathcal{F}$ (with $\mathcal{F} \equiv \{\mathcal{H}, \mathcal{E}, \widetilde{\mathcal{H}}, \widetilde{\mathcal{E}}\}$) defined as

$$\mathcal{F}(\xi,t) = \mathcal{P}\int_0^1 dx \left[\frac{1}{x-\xi} \pm \frac{1}{x+\xi}\right] F_+(x,\xi,t) - i\pi\, F_+(\xi,\xi,t) \qquad (8)$$

where $\mathcal{P}$ denotes the Cauchy's principal value integral, and

$$F_+(x,\xi,t) = \sum_q \left(\frac{e_q}{e}\right)^2 \left[F^q(x,\xi,t) \mp F^q(-x,\xi,t)\right] \tag{9}$$

is the singlet GPD combination for the quark flavor q where the upper sign holds for vector GPDs (H^q, E^q) and the lower sign applies to axial vector GPDs $(\tilde{H}^q, \tilde{E}^q)$. Thus the imaginary part of the CFF accesses GPDs along the diagonals $x{=}\pm\xi$ while the real part probes a convoluted integral of GPDs over the initial longitudinal momentum of the partons. Analytical properties of the $DVCS$ amplitude at the Leading Order (LO) approximation lead to a dispersion relationship between the real and imaginary part of the CFF [Ani07, Die07, Pol08]

$$\Re\mathrm{e}\left[\mathcal{F}(\xi,t)\right] \overset{\text{LO}}{=} D_{\mathcal{F}}(t) + \frac{1}{\pi}\mathcal{P}\int_0^1 dx \left(\frac{1}{\xi - x} - \frac{1}{\xi + x}\right) \Im\mathrm{m}[\mathcal{F}(x,t)] \tag{10}$$

where $D_{\mathcal{F}}(t)$ is the so-called D-term, a t-dependent subraction constant such that [Kum16]

$$D_{\mathcal{H}}(t) = -D_{\mathcal{E}}(t) \quad D_{\widetilde{\mathcal{H}}}(t) = D_{\widetilde{\mathcal{E}}}(t) = 0\,. \tag{11}$$

Originally introduced to restore the polynomiality property of vector GPDs, the D-term [Pol99] enters the parameterization of the non-forward matrix element of the Energy-Momentum Tensor (EMT), which subsequently provides access to the mechanical properties of the nucleon [Pol03, Bur18, Pol18, Kum19]. The independent experimental determination of the real and imaginary parts of the CFF is a key feature for the understanding of nucleon dynamics.

2.3 Beam Charge Asymmetries

Considering the incident lepton $k \equiv (E, \boldsymbol{k})$ scattering into the lepton $k' \equiv (E', \boldsymbol{k'})$ after interaction with an unpolarized proton target at rest $p \equiv (M, \boldsymbol{0})$, the five-fold differential cross section of the $eN\gamma$ process is written

$$\frac{d^5\sigma^e_\lambda}{d^5\Omega} = \Phi_k \, \frac{\mathcal{T}^2_{BH} + \mathcal{T}^2_{DVCS} + \lambda\,\widetilde{\mathcal{T}}^2_{DVCS} + e\,\mathcal{T}_{INT} + e\lambda\,\widetilde{\mathcal{T}}_{INT}}{e^6} \tag{12}$$

where $d^5\Omega{=}dx_B\,dQ^2\,dt\,d\phi_e\,d\phi$ is the hypervolume subtending the elementary solid angle, and

$$\Phi_k = \frac{\alpha^3}{16\pi^2}\,\frac{x_B\,y^2}{Q^4\sqrt{1+\epsilon^2}} \tag{13}$$

is a phase-space factor. The kinematical quantities in Eq. (13) are: $y{=}p{\cdot}q/p{\cdot}k$ and $\epsilon{=}2x_BM/Q$; $q \equiv (\omega, \boldsymbol{q}){=}k - k'$ designates the exchanged virtual photon of squared four-momentum $Q^2{=}\boldsymbol{q}^2 - \omega^2$; additionally, $p' \equiv (E_{p'}, \boldsymbol{p'})$ denotes the recoil proton and $q'{=}q{+}p{-}p'$ represents the final state real photon. The different reaction amplitudes in Eq. (12) can be expressed as a sum of Fourier harmonics [Bel02-1] in terms of the out-of-plane angle ϕ between the leptonic $(\boldsymbol{k}, \boldsymbol{k'})$ and hadronic $(\boldsymbol{p'}, \boldsymbol{q'})$ planes, namely

$$\mathcal{T}^2_{BH} \equiv \frac{1}{\Phi_k}\frac{d^5\sigma_{BH}}{d^5\Omega} = \frac{e^6(1+\epsilon^2)^{-2}}{x_B^2 y^2 t\,\mathcal{P}_1(\phi)\mathcal{P}_2(\phi)} \sum_{n=0}^{2} c_n^{BH}\cos(n\phi) \tag{14}$$

$$\mathcal{T}^2_{DVCS} \equiv \frac{1}{\Phi_k}\frac{d^5\sigma_{DVCS}}{d^5\Omega} = \frac{e^6}{y^2Q^2} \sum_{n=0}^{2} c_n^{DVCS}\cos\left(n\phi\right) \tag{15}$$

$$\widetilde{\mathcal{T}}^2_{DVCS} \equiv \frac{1}{\Phi_k}\frac{d^5\widetilde{\sigma}_{DVCS}}{d^5\Omega} = \frac{e^6}{y^2Q^2} \sum_{n=1}^{2} s_n^{DVCS}\sin\left(n\phi\right) \tag{16}$$

$$\mathcal{T}_{INT} \equiv \frac{1}{\Phi_k}\frac{d^5\sigma_{INT}}{d^5\Omega} = \frac{e^6}{x_B y^3 t\,\mathcal{P}_1(\phi)\mathcal{P}_2(\phi)} \sum_{n=0}^{3} c_n^{INT}\cos\left(n\phi\right) \tag{17}$$

$$\widetilde{\mathcal{T}}_{INT} \equiv \frac{1}{\Phi_k}\frac{d^5\widetilde{\sigma}_{INT}}{d^5\Omega} = \frac{e^6}{x_B y^3 t\,\mathcal{P}_1(\phi)\mathcal{P}_2(\phi)} \sum_{n=1}^{3} s_n^{INT}\sin(n\phi)\,. \tag{18}$$

The $\mathcal{T}^2_{BH}$ amplitude is exactly calculable from the electromagnetic form factors F_1 and F_2 of the proton. All other coefficients feature specific linear or bilinear combinations of CFF. The combinations ($\mathcal{C}^{DVCS}$, $\mathcal{C}^{INT}$) entering the leading twist-2 coefficients (c_0^{DVCS}, c_0^{INT}, c_1^{INT}, s_1^{INT}) of the $DVCS$ and INT amplitudes are

$$\begin{aligned}\mathcal{C}^{DVCS} = {} & 4(1-x_B)\Big(\mathcal{H}\mathcal{H}^\star + \widetilde{\mathcal{H}}\widetilde{\mathcal{H}}^\star\Big) - x_B^2\Big(\mathcal{H}\mathcal{E}^\star + \mathcal{E}\mathcal{H}^\star + \widetilde{\mathcal{H}}\widetilde{\mathcal{E}}^\star + \widetilde{\mathcal{E}}\widetilde{\mathcal{H}}^\star\Big) \\ & -\Big(x_B^2 + (2-x_B)^2\frac{t}{4M^2}\Big)\mathcal{E}\widetilde{\mathcal{E}}^\star - x_B^2\frac{t}{4M^2}\widetilde{\mathcal{E}}\widetilde{\mathcal{E}}^\star \end{aligned} \tag{19}$$

$$\mathcal{C}^{INT} = F_1\mathcal{H} + \xi(F_1+F_2)\widetilde{\mathcal{H}} - \frac{t}{4M^2}F_2\mathcal{E}\,. \tag{20}$$

The $c_{0,1}^{INT}(s_1^{INT})$ coefficients are proportional to the real(imaginary) part of the $\mathcal{C}^{INT}$ combination, and the c_0^{DVCS} coefficient is proportional to the real part of the $\mathcal{C}^{DVCS}$ combination. The other harmonic coefficients correspond either to twist-3 contributions (c_1^{DVCS}, s_1^{DVCS}, c_2^{INT}, s_2^{INT}) or twist-2 double helicity-flip gluonic GPD (c_2^{DVCS}, s_2^{DVCS}, c_3^{INT}, s_3^{INT}). Note that this elegant relationship between twist and harmonic orders, developed in the original work of Ref. [Bel02-1], is distorted by kinematical corrections and target-mass effects [Bel10, Bra14]. This does not impact the present discussion but reaffirms the importance of the separation of the different reaction amplitudes to provide an experimental signal as unambiguously interpretable as possible.

Comparing polarized electron and positron beams, the unpolarized BCA A_{UU}^C can be constructed following the expresssion

$$A_{UU}^C = \frac{(d^5\sigma_+^+ + d^5\sigma_-^+) - (d^5\sigma_+^- + d^5\sigma_-^-)}{d^5\sigma_+^+ + d^5\sigma_-^+ + d^5\sigma_+^- + d^5\sigma_-^-} = \frac{d^5\sigma_{INT}}{d^5\sigma_{BH} + d^5\sigma_{DVCS}} \tag{21}$$

which, at leading twist-2, is proportionnal to the $\Re\mathrm{e}\left[\mathcal{C}^{INT}\right]$ CFF part. It constitutes a selective CFF signal which becomes distorted in the case of the non-dominance of the BH amplitude with respect to the polarization insensitive $DVCS$ amplitude. Similarly, the polarized BCA A_{LU}^C can be constructed as

$$A_{LU}^{C} = \frac{(d^5\sigma_+^+ - d^5\sigma_-^+) - (d^5\sigma_+^- - d^5\sigma_-^-)}{d^5\sigma_+^+ + d^5\sigma_-^+ + d^5\sigma_+^- + d^5\sigma_-^-} = \frac{\lambda\, d^5\widetilde{\sigma}_{INT}}{d^5\sigma_{BH} + d^5\sigma_{DVCS}} \tag{22}$$

$$\neq A_{LU}^{-} = \frac{d^5\sigma_+^- - d^5\sigma_-^-}{d^5\sigma_+^- + d^5\sigma_-^-} = \frac{-\lambda\,(d^5\widetilde{\sigma}_{INT} - d^5\widetilde{\sigma}_{DVCS})}{d^5\sigma_{BH} - d^5\sigma_{INT} + d^5\sigma_{DVCS}} \tag{23}$$

$$\neq A_{LU}^{+} = \frac{d^5\sigma_+^+ - d^5\sigma_-^+}{d^5\sigma_+^+ + d^5\sigma_-^+} = \frac{\lambda\,(d^5\widetilde{\sigma}_{INT} + d^5\widetilde{\sigma}_{DVCS})}{d^5\sigma_{BH} + d^5\sigma_{INT} + d^5\sigma_{DVCS}} \tag{24}$$

which, at leading twist-2, is proportionnal to the $\Im\mathrm{m}\left[\mathcal{C}^{INT}\right]$ CFF part. As A_{UU}^{C}, A_{LU}^{C} is a selective CFF signal affected by the same BH-non-dominance distortion. At leading twist-2 and in the BH-dominance hypothesis, A_{LU}^{C} is simply opposite sign to the Beam Spin Asymmetry (BSA) A_{LU}^{-} (Eq. (23)) measured with polarized electrons, and equal to the BSA A_{LU}^{+} (Eq. (24)) measured with polarized positrons. Therefore, the comparison between A_{LU}^{C}, A_{LU}^{-}, and A_{LU}^{+} provides a handle on the validity of these hypotheses. In the case of significant differences, the neutral BSA

$$A_{LU}^{0} = \frac{(d^5\sigma_+^+ + d^5\sigma_+^-) - (d^5\sigma_-^+ + d^5\sigma_-^-)}{d^5\sigma_+^+ + d^5\sigma_-^+ + d^5\sigma_+^- + d^5\sigma_-^-} = \frac{\lambda\, d^5\widetilde{\sigma}_{DVCS}}{d^5\sigma_{BH} + d^5\sigma_{DVCS}} \tag{25}$$

allows us to distinguish which hypothesis may not be fulfilled.

Unpolarized and polarized BCA observables are shown on Fig. 3 (top panel) for a selected set of kinematics within CLAS12 acceptance and a 10.6 GeV beam energy. They are determined using the BM modeling of DVCS observables [Bel10] and the KM CFF [Kum10]. The sensitivity to the CFF model is also shown on Fig. 3 (bottom panel) where observables calculated for 3 typical kinematics using PARTONS [Ber18] CFF and a choice of VGG [Van99] CFF are compared to previous evaluations.
The amplitude of A_{UU}^{C} strongly depends on kinematics and varies not only in magnitude (within $\pm 30\%$) but also in shape, exhibiting a dominant $\cos(\phi)$ contribution eventually distorted by $\cos(2\phi)$ contributions originating from the unpolarized part of the DVCS cross section. Similarly, the polarized BCA corresponding to the same kinematics also varies in magnitude (15%-35%) and shape, eventually showing a distorsion of the dominant $\sin(\phi)$ contribution by the $\cos(n\phi)$ dependence of the unpolarized DVCS cross section. A strong sensitivy of the the magnitude of A_{UU}^{C} to the CFF model is also shown (bottom panel of Fig. 3), confirming the importance of BCA observables for the extraction of the real part of the interference CFF. The dominance of the $\sin(\phi)$ modulation from the imaginary part of the interference CFF in A_{LU}^{C} is also observed with a magnitude sensitive to the CFF model. This supports the expected *purity* of this observable for the extraction of the imaginary part of the interference CFF.

Using a polarized positron beam, further observables can be extracted and compared with polarized electron beam observables. Particularly, the positron BSA, a golden experimental observable minimizing acceptance and efficiency effects, can be compared with the electron BSA and the polarized BCA. From Eq. 22-24

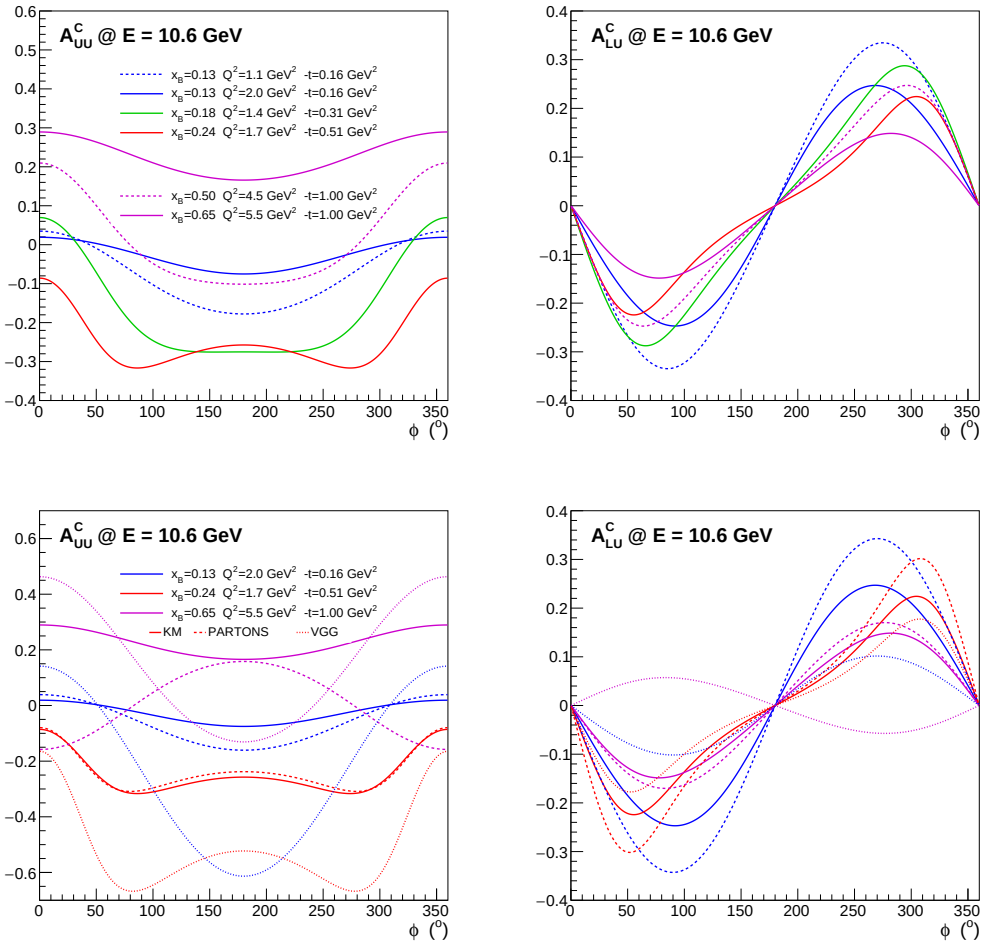

Figure 3. Kinematic dependence of unpolarized (top left) and polarized (top right) BCA at a beam energy of 10.6 GeV, and CFF model sensitivity of observables (bottom panel) for selected kinematics.

$$\frac{A^+_{LU}+A^-_{LU}}{2}=\lambda\,\frac{d^5\tilde{\sigma}_{DVCS}\left(d^5\sigma_{BH}+d^5\sigma_{DVCS}\right)-d^5\tilde{\sigma}_{INT}d^5\sigma_{INT}}{\left(d^5\sigma_{BH}+d^5\sigma_{DVCS}\right)^2-\left(d^5\sigma_{INT}\right)^2} \tag{26}$$

$$A^C_{LU}-A^+_{LU}=\lambda\,\frac{d^5\tilde{\sigma}_{INT}d^5\sigma_{INT}-d^5\tilde{\sigma}_{DVCS}\left(d^5\sigma_{BH}+d^5\sigma_{DVCS}\right)}{\left(d^5\sigma_{BH}+d^5\sigma_{DVCS}\right)\left(d^5\sigma_{BH}+d^5\sigma_{INT}+d^5\sigma_{DVCS}\right)} \tag{27}$$

which, within the BH dominance hypothesis, provides the relationship

$$A^C_{LU}=\frac{A^+_{LU}-A^-_{LU}}{2}\,. \tag{28}$$

Fig. 4 shows the positron BSA (bottom left), the comparison bewteen positron and electron BSA (middle left) and the deviation from the BH dominance hypothesis (top left) for the previous selected set of kinematics. The magnitude of A^+_{LU} strongly depends on kinematics and exhibits a dominant $\sin(\phi)$ contribution. The comparison between positron and electron BSA, expressed in terms of the BSA sum, shows the expected ϕ-modulation in absence of higher

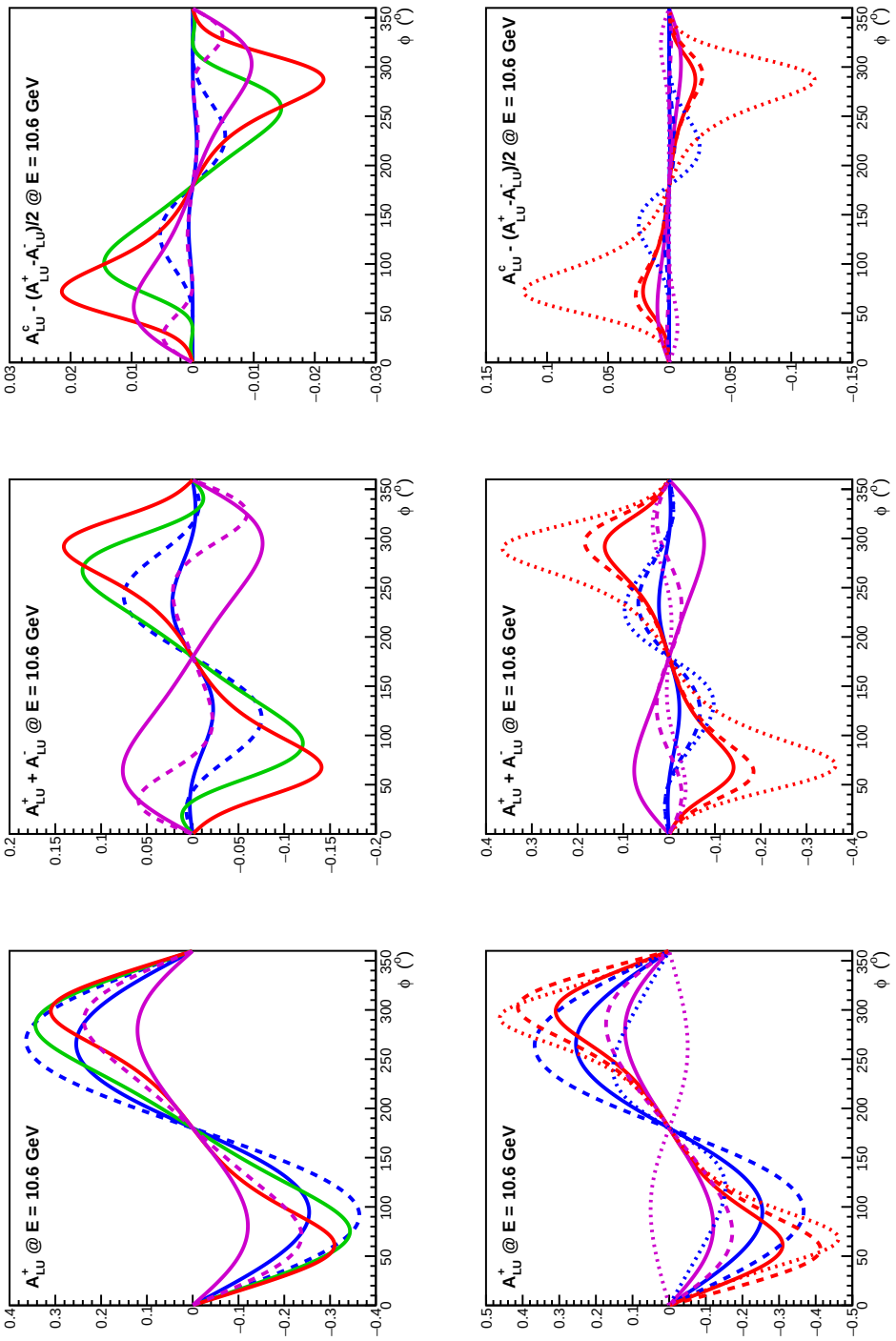

Figure 4. Kinematic dependence of the positron BSA A^{+}_{LU} (bottom left), the comparison A^{+}_{LU}+A^{-}_{LU} between electron and positron BSA (middle left), the deviation A^{C}_{LU}-(A^{+}_{LU}-A^{-}_{LU})/2 from the BH dominance hypothesis (top left) at a beam energy of 10.6 GeV, and CFF model sensitivity of observables (right panel) for selected kinematics. Curves label are identical to Fig. 3.

twist contributions. Both A_{LU}^{+} and the BSA sum are strongly sensitive to the CFF model (right panel of Fig. 4). The deviations from the BH dominance hypothesis are generally small but may become sizeable depending on the CFF scenario.

3 Impact of positron measurements

The importance of BCA observables for the extraction of CFF has been stressed numerous times in the literature (see among others [Bel02-1], [Die03], or [Bel05]). Indeed, at leading twist-2 this problem can be seen as the determination of 8 unknown quantities (4 $\Re\mathrm{e}\,[\mathcal{F}]$ and 4 $\Im\mathrm{m}\,[\mathcal{F}]$) from a non-linear sytem of coupled equations [Gui08] which requires at a minimum 8 independent experimental observables with different sensitivities to the unknwon quantities. Dispersion relations and sum rules bring correlations bewteen CFF and links with elastic and deep inelastic experimental data, but the problem is generally complex and requires a large set of experimental observables. Not to forget that higher twist effects and NLO corrections render the extraction even more difficult. Nevertheless, existing data about DVCS with lepton beams of opposite polarities are limited and restricted to the H1 [Aar09], HERMES [Air08, Air09, Air12] and COMPASS [Akh19] experiments which explored a kinematical domain very different from the valence domain accessible at JLab.

The methods for the extraction of CFF from DVCS observables can be classified in two generic groups: GPD-model independent [Gui08, Kum11, Mou19] and dependent [Kum08, Kum10] methods. Both methods are still depending on the cross section model (leading twist, target mass corrections, higher twist, NLO corrections...) and of further fitting hypotheses like the number of CFF to be extracted from data. In that sense, the quantitative evaluation of the impact of positron measurements discussed in this section is necessarily model dependent.

Observable	σ_{UU}	A_{LU}	A_{UL}	A_{LL}	A_{UU}^{C}	A_{LU}^{C}
Time (d)	80	80	100	100	80	80
$\mathcal{L}$ ($\times 10^{35}$ cm$^{-2}\cdot$s^{-1})	0.6	0.6	2	2	0.6	0.6
Packing Fraction	1	1	0.17	0.17	1	1
Sytematics (%)	5	3	3	3$\oplus$3	3	3

Table 1. Parameters of simulated observables.

The study developed here-after is an attempt to evaluate the benefit of unpolarized and polarized BCA measurements off an unpolarized hydrogen target. This evaluation is quantified with respect to the CFF extraction performed using a local fit of already approved CLAS12 p-DVCS measurements with or without BCA data. In absence of completed analysis or actual today existence of experimental data, we consider the parameters of approved CLAS12 DVCS

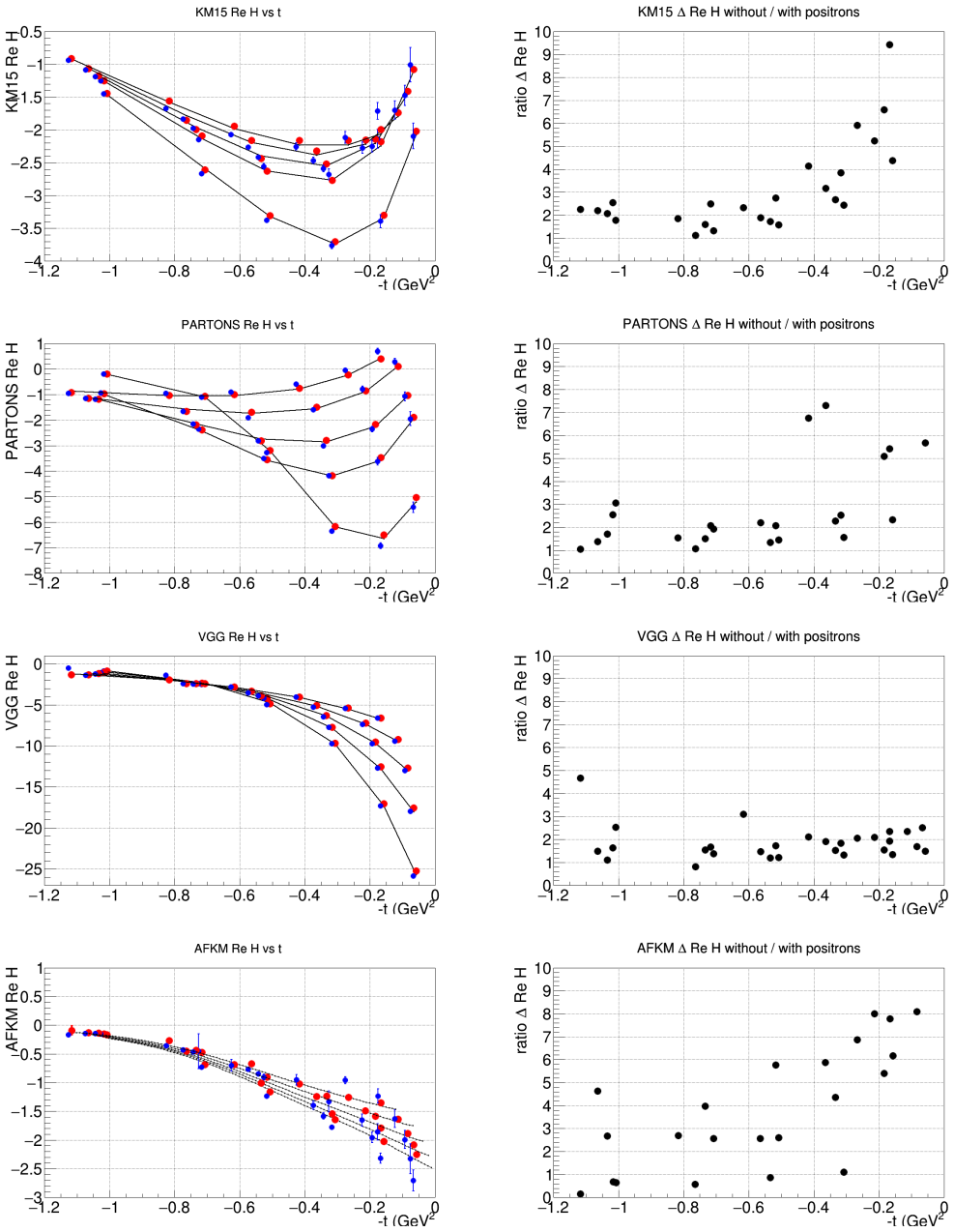

Figure 5. Impact of the positron data on the extraction of $\Re e[\mathcal{H}]$ with four different CFF model scenarios: projection of extracted $\Re e[\mathcal{H}]$ without (blue points) and with (red points) positron data compared to the model value (line); ratios of errors on the extracted $\Re e[\mathcal{H}]$ with positron data with respect to electron data only (right). The blue points are slightly shifted in x for visual clarity.

experiments using a polarized electron beam with an unpolarized and longitudinally polarized proton target. Without impact on the extraction of $\mathcal{H}$, the transversely polarized target is not considered in this evaluation.
Within a first approach, observables are determined for a 10.6 GeV beam energy using the BM modeling of the cross section [Bel10] combined with different CFF [Van99, Kum10, Asc13, Ber18]. The projected statistical errors are obtained from the parameters of Tab. 1, where the packing fraction represents

a luminosity reduction factor, of relevance for the polarized target. The CFF $\mathcal{H}$ and $\widetilde{\mathcal{H}}$ are then simultaneously extracted from projected data using a fitting procedure which assumes the model values for the non-fitted CFF. Individual observables are randomly smeared with the projected statistical uncertainties, and systematically shifted with the projected systematic uncertainties before CFF fitting. These two steps combined into uncertainties on the extracted CFF. The results of the procedure repeated with 4 different CFF models are summarized in Fig 5. The left column shows the model $\Re\mathrm{e}[\mathcal{H}]$ as a function of $-t$ for different (x_B, Q^2) bins (line), together with the extracted values without (blue points) and with (red points) the positron data. The corresponding set of plots on the right column shows the ratios of the total uncertainties, statistical and systematical added in quadrature. The impact of the positron data is found to be particularly strong at small -t where they can decrease uncertainties on $\Re\mathrm{e}[\mathcal{H}]$ by over a factor five. The electron data only scenario tends to provide values different from the model values. By providing a pure interference signal, positron data corrects for this deviation and allows the fitting procedure to recover the input model value.

4 Polarized positron beam production and transport

The prospect of polarized or unpolarized positron beams for nuclear physics experiments at CEBAF naturally raises several issues. Prominent among these are the generation of positrons, their formation into beams acceptable to the 12 GeV CEBAF accelerator, and the technical challenges associated for the magnetic transport and diagnostics of low current positively charged beams. The following sections summarize the present thinking towards developing positron beams and address some of the specfic issues of positron beams at CEBAF and in Hall B.

4.1 Polarized positron source

Polarization phenomena in electromagnetic processes have been investigated since the early thirties [Som31, Wic51, May51]. The originally more complete calculations of the polarization of the bremsstrahlung radiation generated by an electron beam in a nuclear field environment [Ols59] drove the development of polarized photon beams: an unpolarized electron beam generates a linearly polarized photon beam, while a polarized electron beam generates a circularly polarized photon beam with polarization directly proportionnal to the initial electron beam polarization. These features were used extensively at numerous accelerator facilities, for instance in Hall B [Mec03] to operate a high energy polarized photon beam.
As a reciprocal process to bremsstrahlung, polarization observables of the pair creation process behaves symmetrically to bremsstrahlung: particularly, the circular polarization of a photon beam is predicted to transfer into longitudinal and transverse polarization components of the e^+e^--pair [Ols59, Kur10], both proportionnal to the initial photon beam polarization. Polarization transfer

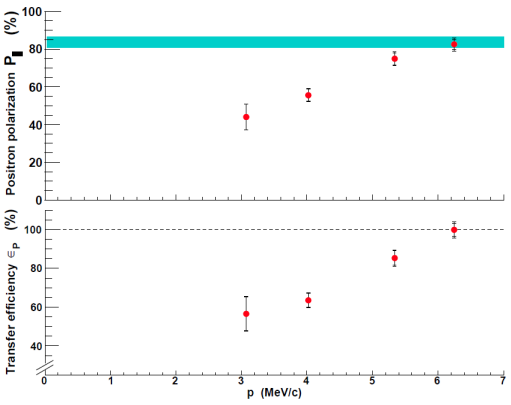

Figure 6. PEPPo measurements of the positron polarization (top panel) and polarization transfer efficiency (bottom panel); statistics and systematics are reported for each point, and the shaded area indicates the electron beam polarization [Abb16].

in the transverse plane is however much less efficient than in the longitudinal plane such that the pair is essentially longitudinally polarized. The experimental demonstration of the circular-to-longitudinal polarization transfer is relatively recent and has been carried out at KEK [Omo06], SLAC [Ale08] and JLab [Abb16] using different techniques to produce the polarized photon beam: Compton back-scattering of polarized laser light off a ∼GeV electron beam [Omo06], polarized synchroton radiation of a multi-GeV electron beam traveling within a helical undulator [Ale08], and bremsstrahlung radiation of a polarized electron beam [Abb16]. The experimental demonstration [Gra11] of the latter technique (so-called PEPPo) was worked-out at the CEBAF injector using a 8.19±0.04 MeV/c highly polarized electron beam. The PEPPo experiment reported a very efficient momentum-dependent polarization transfer (Fig. 6), reaching 100% in the high momentum part of the positron spectra. Operating efficiently with a low energy (∼10-100 MeV/c), high intensity (∼mA), and high polarization ($>$ 80%) electron beam driver, the PEPPo technique is ideally suited for the production of polarized positron beams at CEBAF.

A PEPPo based polarized positron source can be sketched as a conventional positron source operating instead with a polarized electron beam and involving positron energy discrimination: selecting high energy positrons favors high spin polarization but reduced the beam intensity, while the selection of low energy positrons maximizes the beam intensity at the expense of a reduced polarization. The optimization of a positron source is a sophisticated problem combining several physics and technological parameters. As a rule of thumb, an optimum operation in polarization mode can be obtained at half of the energy of the incoming electron beam energy and typically provides 75% polarization transfer efficiency. The trade between polarization and intensity capabilities is illustrated on Fig. 7 showing the simulated peformance of a positron source using a 123 MeV and 100% polarized electron beam. A software collimator combining a 1 MeV energy acceptance and alternatively a 10° angular acceptance or a 10 mm·mrad emittance mimics the positron collection efficiency. The latter configuration corresponding to the measured emittance acceptance of CEBAF [Gol10] strongly affects the energy dependence of the

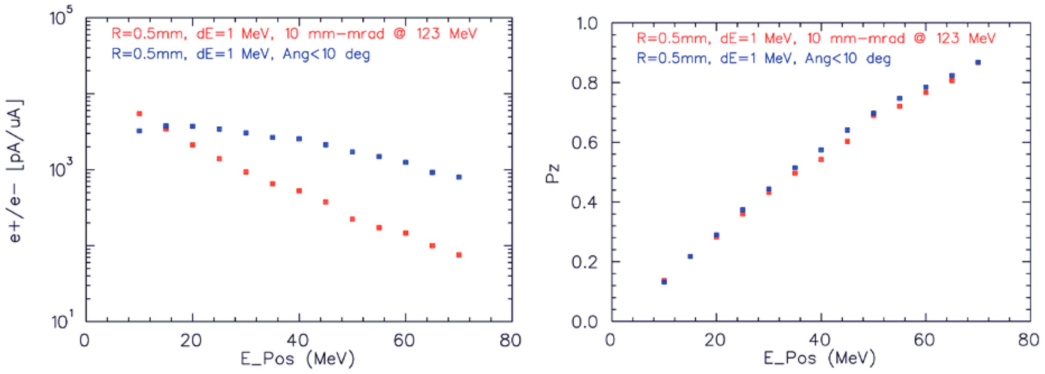

Figure 7. Energy dependence of the positron efficiency production (left) and polarization transfer efficiency $P_z \equiv P_z/P_e$ (right) simulated with a 123 MeV and 100% polarized electron beam [Car18]. Points correspond to the selection of produced positrons within an energy spread of 1 MeV and a constant angular acceptance of 10° (blue) or a 10 mm·mrad emittance (red).

positron production efficiency. Considering a 1 mA initial electron beam, the simulated positron beam intensity decreases from 5 μA down to 100 nA in the 10-60 MeV positron energy range, while the polarization increases from 10% up to 75%. Within the PEPPo scheme, the energy of the selected positrons is indeed defining the capabilities of the positron source.

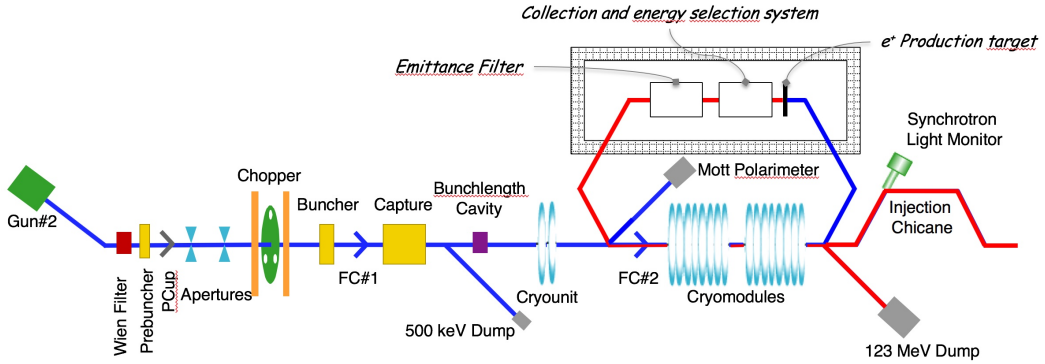

Figure 8. An approach to adding positron capability to CEBAF [Car18].

While the final scheme of positron beam implementation at CEBAF will result of a multi-parameter optimization, the initial intent of the positron source development effort is to stay in the energy range of the CEBAF injector. A possible configuration is represented on Fig. 8. A high intensity and highly polarized electron beam produced at the head-start of the CEBAF injector is accelerated up to 123 MeV and transported outside of the existing accelerator tunnel towards a new close-by area dedicated to positron production. The main components of the source are a high power target, a magnetic collection system, and a RF-cavity system to match the positron source emittance with CEBAF acceptance.

4.2 CEBAF operation with positron beams

The operation of CEBAF with positron beams was extensively discussed in the LOI12-18-004 [Gra18]. Main challenges are briefly reported hereafter and a broader discussion can be found in Appendix B.

Magnet polarity reversal

In order for positrons to transit CEBAF in the usual electron path, all magnetic fields must be inverted in polarity. The dipole powering network uses common power supplies feeding strings of magnets in series. Magnets were designed to be slightly too high in field strength, and electronic loads (*shunts*) are installed to shunt a controlled amount of the current. All machine protection provisions for the dipole magnets remain functional with the main power supply leads inverted. The shunt hardware is unipolar, and inverting the shunt leads in coordination with the power supply leads leaves the dipole powering network fully functional and protected.
These many power supplies and shunt connections require reversing switches (see Appendix B) to be installed with carefully designed features added to ensure that all polarity changes remain appropriately coordinated.

Beam diagnostic capabilities

Operation of CEBAF requires diagnostics to configure the beam position along the accelerator, typically a combination of non-intercepting diagnostics (Beam Position Monitors (BPM) and Synchrotron Light profile Monitors (SLM)) and intercepting viewscreens. Finer quantitative measurement of the beam size on target and for configuration of accelerator optics is done using either wire scanners for profile measurement or SLM in some cases. In the case of instability of accelerating RF or of steering of focusing magnets, the accelerator is protected from damage by a combination of photomultiplier based beam loss monitors (BLM) and a Beam Loss Accounting system (BLA) which compares the injected current to that delivered to the user(s). Current investigations show that the operation of these systems with positron beams do not raise any difficulty (see Appendix B).

For very low current beam delivery to Hall B, it has been found adequate to configure the accelerator systems with low duty-factor beam with higher peak current, and then turn the beam current down to nanoAmpere levels of continuous wave (CW) current to conduct experiments. This is expected to remain practical for low-current positron operation, although improvements in diagnostics should enable more extensive monitoring of the beam in the accelerator.

Area	δp/p [x10^{-3}]	ε_x [nm]	ε_y [nm]
Chicane	0.5	4.00	4.00
Arc 1	0.05	0.41	0.41
Arc 2	0.03	0.26	0.23
Arc 3	0.035	0.22	0.21
Arc 4	0.044	0.21	0.24
Arc 5	0.060	0.33	0.25
Arc 6	0.090	0.58	0.31
Arc 7	0.104	0.79	0.44
Arc 8	0.133	1.21	0.57
Arc 9	0.167	2.09	0.64
Arc 10	0.194	2.97	0.95
Hall D	0.18	2.70	1.03

Area	δp/p [x10^{-3}]	ε_x [nm]	ε_y [nm]
Chicane	10	500	500
Arc 1	1	50	50
Arc 2	0.53	26.8	26.6
Arc 3	0.36	19	18.6
Arc 4	0.27	14.5	13.8
Arc 5	0.22	12	11.2
Arc 6	0.19	10	9.5
Arc 7	0.17	8.9	8.35
Arc 8	0.16	8.36	7.38
Arc 9	0.16	8.4	6.8
MYAAT01	0.18	9.13	6.19

Figure 9. Comparison of simulated electron and positron beam properties [Rob17]. The light blue arrow indicates the prominence of acceleration damping effects, and the light orange ones corresponds to the dominance of the effects of synchrotron radiations.

Positron beam characteristics

The injection chicane properties (aperture and dispersion) control the CEBAF beam acceptance. These are normally configured for low emittance and low momentum spread beams, but the configuration has considerable flexibility. For instance, the chicane dispersion can be configured to accept up to 2% momentum dispersion and for the low currents anticipated for positron operation, the acceptable RMS beam radius may be as high as several mm matching with a normalized emittance acceptance of 40 mm·mrad for beam energies ∼120 MeV. Because this principal limiting aperture is very localized, it can be readily modified to increase its acceptance. After injection, the beam momentum is increased by a factor of 9 in the first linac (the North Linac). The result of this strong adiabatic damping is that the momemtum acceptance of the accelerator is dominated by the injection chicane. The transverse emittance is similarly strongly damped, and the injection chicane again provides the principal limitation.
Estimated beam parameters are shown in Fig. 9 comparing electron and positron beam optical parameters from the injector entrance till experimental halls. Two main regimes are affecting the beam properties: the acceleration damping within the CEBAF accelerating sections, and the synchrotron radiation in the recirculating arcs. In that respect, the dynamics of the momentum spread of electron beams is dominated by radiation effects. Despite a much larger initial momentum spread, positron beams essentially benefit from acceleration damping which results in the same momentum spread than electron beams. The large positron beam emittance at the injector entrance is also strongly reduced by acceleration effects which result in a final emittance 4-5 times larger than electron beam one's.

4.3 Positron beam operation in Hall B

The positron beam transport through the Hall B beam line in general is no different from the electron beam other than the opposite charge. Once the polarity of all magnetic elements is reversed the positrons will follow exactly the same trajectory as electrons. All magnets in the beam line are equipped with bi-polar power supplies. The emittance of the positron beam is expected to be larger than electron beam. This will require additional focusing of the beam to reduce the beam spot size on the target which will be done with a set of quadrupoles already installed on the beam line but not used with electron beam.

There are some differences related to beam diagnostic devices like BCMs, BPMs and Faraday cup. Their signals will have the opposite sign compared with electron beam operation but this does not pose a problem (see Appendix B). However, there is a significant difference in the beam polarimetry for electron and positron beams. The existing Hall B polarimeter is configured for Møller scattering. With the positron beam it must be reconfigured to accomodate Bhabha scattering. The details of possible solutions are discussed in the Appendix A.

4.4 Monte Carlo simulations of background

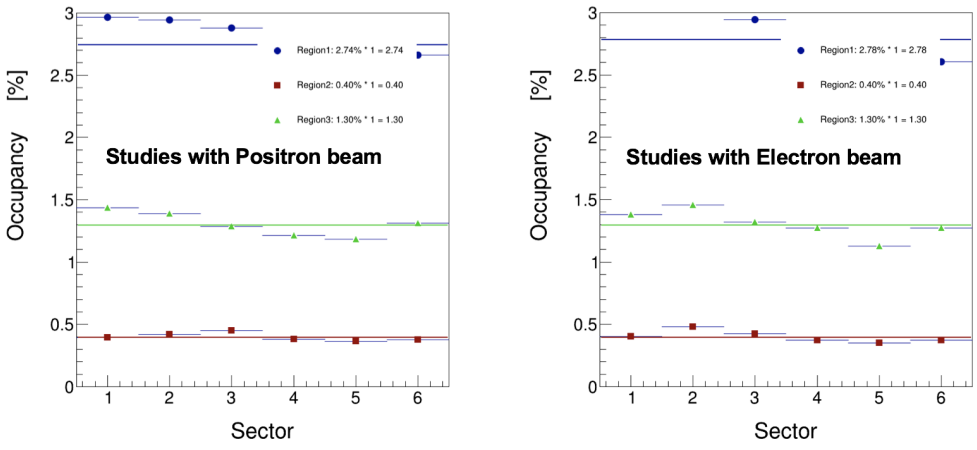

Figure 10. Results for CLAS12 drift chambers occupancy obtained from GEANT simulations with positron and electron beams at a luminosity of $10^{35}\text{cm}^{-2}\text{s}^{-1}$.

A critical part of operating CLAS12 detector at high luminosities is the simulation not only of hadronic events but also, and more importantly, the simulation of beam-related accidental hits in the CLAS12 detector systems, in particular the tracking devices. Source of accidentals in this experiment is primarily from the positron elastically scattering off atomic electrons (Bhabha scattering) and their secondary interaction with beamline components. The production rate of this background sources is orders of magnitude larger than the hadronic production rate. In the case of CLAS12 experiments with electron beam, the

source of accidentals is primarily from beam electrons undergoing Møller scattering off atomic electrons in the liquid hydrogen target. The shielding of the CLAS12 detector from this background was carefully and extensively studied during the CLAS12 design and construction. The final solution of the shielding was obtained by combination of magnetic shielding from the CLAS12 5 T superconducting solenoid and carefully optimized design and fabrication of the Møller absorber. This allowed us to operate CLAS12 at the design luminosity on day one. In studying the background for this experiment, detailed GEANT simulation were performed based on the CLAS12 realistic simulation package used for electron beam at luminosity of $10^{35}\text{cm}^{-2}\cdot\text{s}^{-1}$ reversing the Torus field with respect to the electron beam configuration (in-bending mode). We performed detailed comparison of the drifts chambers occupancy with results obtained with electron beam at the same luminosity taking into account the correct DC time windows of each region. The summary results of the simulation of the drift chamber occupancies are shown in figure 10. Region 1 has the highest occupancy of about 3%, region 2 is about 0.8%, and region 3 is about 1.2%. These results are compatible with the ones obtained with electron beam.

In summary, no additional shielding is needed for this experiment, and we can switch between running the experiment with positrons and electrons keeping the CLAS12 configuration and the operating luminosity, the same. Additionally, a realistic simulation package is essential for absolute normalization, especially, to take into account the detector occupancies for data taking at a given luminosity. In order to quantitatively account for this, pre-scaled trigger bits will be setup to take randomly triggered data simultaneously with the production data. Then in the offline data analysis we will merge DVCS simulation event with random triggered events from data to evaluate tracking and particle identification efficiency for absolute cross section measurements.

5 p-DVCS at CLAS12 with a positron beam

5.1 Detector configuration

The experiment will measure the DVCS process $e^+p \to e^+p\gamma$ with the CLAS12 spectrometer. The arrangement of CLAS12 in the Hall B is shown in a side view in Fig. 11, and the beam line upstream and downstream of CLAS12 are shown in Fig. 12 (see Ref. [Bur20] for details). When operating with positron beam the experiment will use the standard Hall B beam line with the electrical diagnostics in reversed charge mode from operating the beam line and the experimental equipment with electron beam. This includes the nano-ampere beam position and current monitors, the beam line magnetic elements including the tagger magnet, which is energized during beam polarization measurements, and the charge integrating Faraday cup. The experimental setup will be identical to the standard electron beam setup with both magnets, the Solenoid and the Torus magnet in reversed current mode from electron scattering experiments.

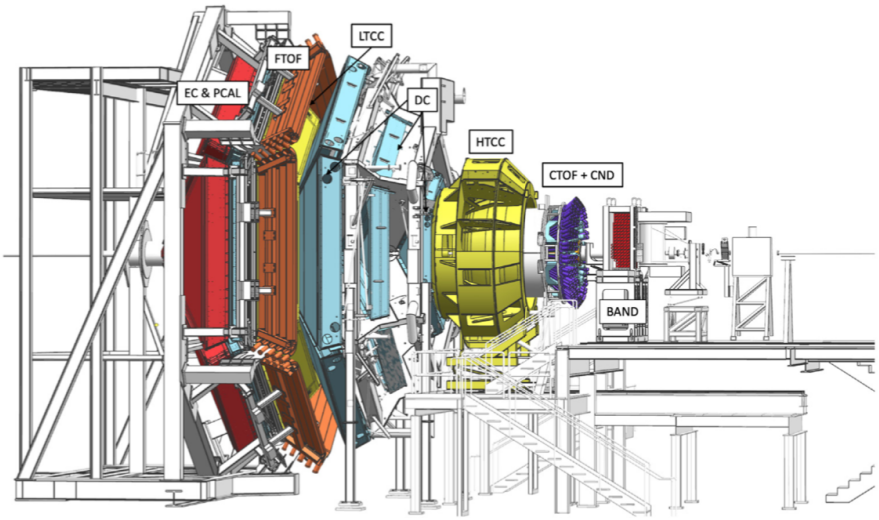

Figure 11. CLAS12 in Hall B. The positron beam comes from the right and hits the target in the center of the solenoid magnet, which is at the core of the Central Detector (CD). It is largely hidden from view inside the HTCC Čerenkov counter.

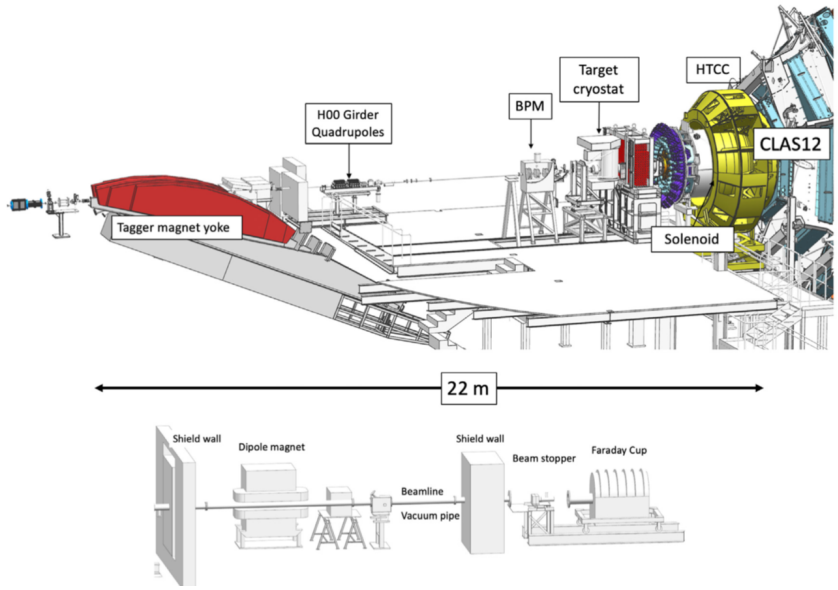

Figure 12. Hall B beamline.

As the positron beam emittance at the target will be larger than in standard electron beam operation from the later driven gun, the liquid hydrogen target cell will be redesigned with increased entrance and exit window size of the target cell.

5.2 Kinematic coverage

The simultaneous kinematic coverage of the DVCS process in the CLAS12 acceptance is shown in Fig. 13 from a subset of Run Group A (RGA) data and a

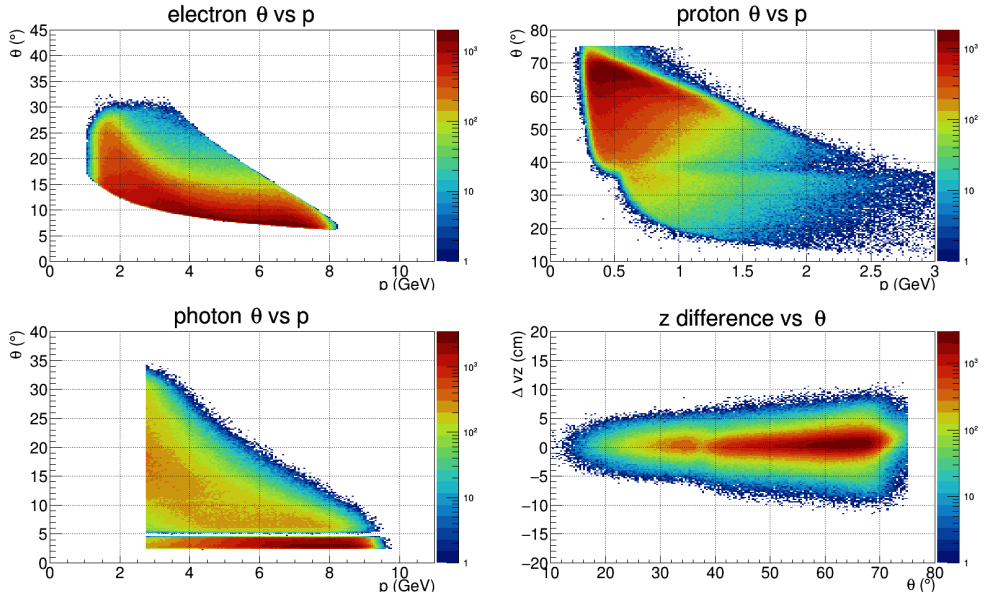

Figure 13. Kinematic coverage of CLAS12 for exclusive DVCS events at a beam energy of 10.6 GeV: scattered lepton reconstruction coverage in polar angle versus momentum (top left); proton reconstruction coverage in polar angle versus momentum (top right); at polar angles close to 40°, protons are partially reconstructed in the FD and partially in the CD; high-energy photon detection coverage in polar angle versus photon energy (bottom left); the narrow band below 5° indicates photon detection in the FT calorimeter; difference in reconstructed z-vertex for scattered leptons and the recoil protons (bottom right).

detector configuration similar to the positron configuration *i.e.* Torus in Out-Bending mode and FTCal ON. Scattered electrons/positrons will be detected in the CLAS12 Forward Detectors including the high threshold Čerenkov Counter (HTCC), the drift chamber tracking system, the Forward Time-of-Flight system (FTOF) and the electromagnetic calorimeter (ECAL). The latter consists of the pre-shower calorimeter (PCAL) and the EC-inner and EC-outer parts of the electromagnetic calorimeter (EC) providing a 3-fold longitudinal segmentation. DVCS photons are measured in the CLAS12 ECAL that covers the polar angle range from about 5° to 35°. Additionally, high energy photons are also detected in the Forward Tagger calorimeter FTCal, which spans the polar angle range of 2.5° to 4.5°. Protons are detected mostly in the CLAS12 Central Detector (CD) with momenta above 300 MeV/c, but a significant fraction is also detected in the CLAS12 Forward Detector, especially those in the higher $-t$ range.

The kinematics coverage is shown in Fig. 14. Scattered leptons cover the x_B range from 0.1 to 0.7 and a range in Q^2 from 1 to 10 GeV^2. The range in $-t$ covers 0.05 to 2.5 GeV^2.

In Fig. 15 we show the event distribution in the individual FD sectors, the eγX missing mass distribution with all particles detected, and the ϕ-distributions of exclusive events.

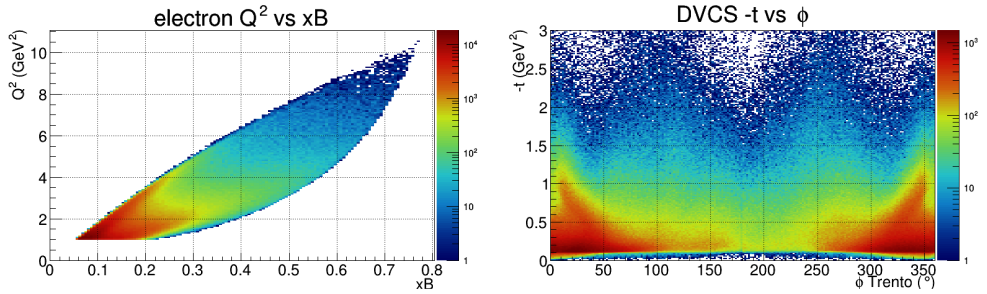

Figure 14. Kinematic coverage of exclusive DVCS/BH events in Q^2 versus x_B (left), and in $-t$ (right) plotted versus the azimuthal ϕ-dependence.

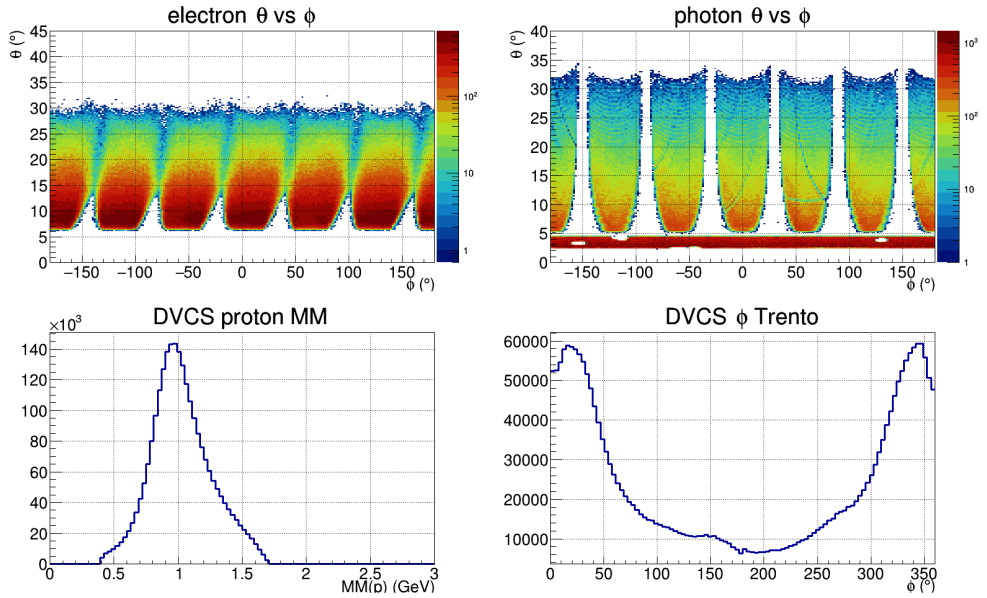

Figure 15. DVCS/BH event distributions in individual Torus sectors: lepton ϕ-distribution versus polar angle (θ) (top left), showing a slightly slanted asymmetric distribution due to the solenoid magnetic field; high energy photon distribution (top right), showing the ECAL (PCAL+EC) coverage at $\theta > 5^\circ$ and the FT calorimeter coverage at $\theta < 5^\circ$; the eγX missing mass distribution, peaking at the proton mass (bottom left), with the radiative tail on the high mass side; the azimuthal distribution of DVCS events (bottom right).

6 Control of systematic uncertainties

6.1 Origin of systematic effects

Systematic effects can occur on the one hand from positron beam properties, and on the other hand from the response of the CLAS12 spectrometer.

The expected positron beam properties in the physics interaction region differ from the CEBAF electron beam essentially by a 4-5 times larger emittance (see Sec. 4.2). Additional focusing of the beam will be provided by a set of quadrupoles already installed on the beam line but residual effects of the beam

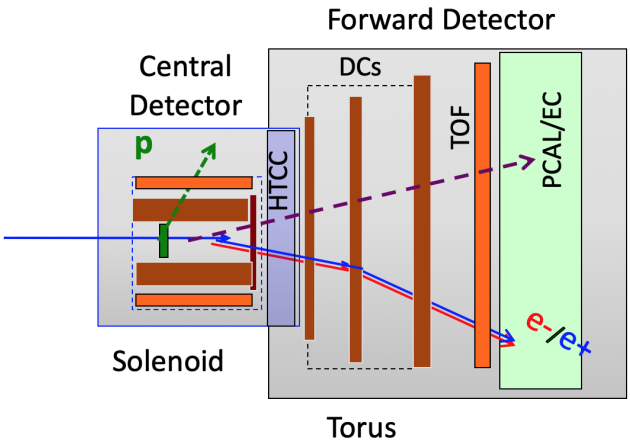

Figure 16. The generic setup of the CLAS12 detector in Hall B in a side view. For the same kinematics the forward going particles electrons and positrons are following the same path for reversed polarity of the Torus magnet and the solenoid magnet (both bending away from the beam line).

properties difference may remain which could alter the comparison with electron data. To control these effects DVCS data with an electron beam having the same properties as the positron beam should be carried out. Such beam can be made out of the secondary electrons produced at the positron source, which is expected to have similar properties in terms of (x, y) profile and emittance at the target position. This will allow for the elimination/correction of potential beam-related false asymmetries.

Systematic uncertainties for DVCS cross section measurements with electron beams are part of the currently ongoing program with the CLAS12 spectrometer setup. For positron beams most of these systematic effects are very similar as far as the CLAS12 detector properties and normalization issues are concerned. As we aim for measurements of charge differences in cross sections or charge asymmetries most of them will be identical and will therefore drop out in the difference of electron and positron measurements. There are a few effects that however may not drop out and have to be considered.

The experimental setup is generically shown in a side view in Fig. 16, and in Fig. 17 in a view along the beam line looking downstream. For the scattered positron and for the DVCS photon the detector looks identical to the situation when electrons are scattered off protons and the magnetic fields in both magnets are reversed. Additional software fiducial cuts will further ensure the same detector status between electron and positron data taking for these particles driving the resolution of the DVCS analysis. This is not the case of the recoil proton, which will be bent in the solenoid field in the opposite direction compared to the electron scattering case. This could result in systematic effects due to potentially different track reconstruction efficiencies and effective solid angles. While these effects are much smaller than the physics asymmetry (see Sec. 2.3), we propose here to measure the positron DVCS process 50% of the time with reversed solenoid polarity so that the proton will bend half

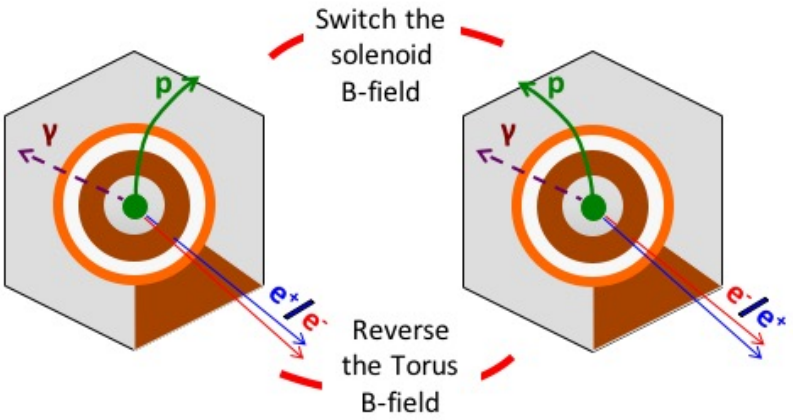

Figure 17. The generic setup of the clas12 detector in Hall B viewed from upstream down the beam pipe. In this view the proton rotates in the opposite direction, from the case of the electron beam. When swithing the solenoid field the electron and positron experience different phi motions due to the opposite motion of electron and positrons (left). When the solenoid field is reversed the electrons and positrons get kicks in the opposite azimuthal directions as seen that positrons and electrons switch place in the forward detector. This potential asymmetry can be controlled with elastic scattered electrons and positrons.

time in one direction and half time in the opposite direction.
Another cross check is possible by measuring the elastic $e^+p \to e^+p$ scattering cross section continuously during the experiments. The CLAS12 acceptance covers elastic scattering and deep inelastic processes, such as DVCS, and both will be measured concurrently. In either case most of the recoil protons are detected in the central detector, giving us continuous control of the performance of the detector system throughout the experiment. It should be noted that the elastic $e^+p \to e^+p$ cross section is equal to the well known elastic $e^-p \to e^-p$ cross section within the contributions from 2-photon effects, which are very small in the kinematic range that can be selected for the process [Afa17].

The charge asymmetries for the DVCS process can be large (see Sec. 2.3). From the simulation calibrated by the measurement of known processes, we aim at keeping systematic uncertainties due to these effects below 3% at all kinematics. We also note that for the positron beam spin asymmetry, which will be measured concurrently, the systematic uncertainties are not affected by the aforementioned electron-positron differences.

6.2 Beam charge asymmetry systematics

The unpolarized Yield Charge Asymmetry (YCA) is defined experimentally as

$$\mathcal{Y}^C_{UU} = \frac{(Y^+_+ + Y^+_-) - (Y^-_+ + Y^-_-)}{Y^+_+ + Y^+_- + Y^-_+ + Y^-_-} \tag{29}$$

where

$$Y^e_\lambda = \frac{N^e_\lambda}{Q^e_\lambda}\frac{1}{\epsilon^e} = \frac{n^e_\lambda}{\epsilon^e} \tag{30}$$

is the beam charge and spin dependent normalized yield determined from the number of events N^e_λ, the corresponding accumulated charge Q^e_λ, and the beam spin independent detector efficiency ϵ^e. Comparing electron and positron measurements taken at different time periods, the detector efficiency will most likely be different. Noting this difference $\Delta\epsilon$, the efficiency correction factor is defined as

$$C_\epsilon = \frac{1}{2}\frac{\Delta\epsilon}{\epsilon^+} = \frac{1}{2}\frac{\epsilon^+ - \epsilon^-}{\epsilon^+}\,. \tag{31}$$

Additionally, systematic differences in acceptance between electron and positron beams may occur which translate into an excess/deficit of positron events as compared to the true physics event number expected within the acceptance of electron beam data. Noting δn^0_0 the spin and charge independent positron excess, the charge normalized yield for electrons and positrons can be expressed as

$$n^-_\pm = n^0_0\left(1 - A^C_{UU}\right)\left(1 \pm A^-_{LU}\right) \tag{32}$$

$$n^+_\pm = n^0_0\left(1 + \frac{\delta n^0_0}{n^0_0}\right)\left(1 + A^C_{UU}\right)\left(1 \pm A^+_{LU}\right) \tag{33}$$

where the BCA and the BSA quantifies the charge and spin dependences of the yield. Here,

$$n^0_0 = \frac{n^+_+ + n^+_- + n^-_+ + n^-_-}{4} \tag{34}$$

is the unpolarized charge normalized neutral yield. The solid angle correction factor can be defined as

$$C_{\Delta\Omega} = \frac{1}{2}\frac{\delta n^0_0}{n^0_0} = \frac{1}{2}\frac{\Delta\Omega^+ - \Delta\Omega^-}{\Delta\Omega^-} \tag{35}$$

where $\Delta\Omega^+$ is the solid angle for the positron data taking, and $\Delta\Omega^-$ is the solid angle for the electron data taking. The true unpolarized BCA, taking into account efficiency and solid angle corrections, can be derived from the experimental YCA following the expression

$$A^C_{UU} = \frac{(1+\eta_c)\,\mathcal{Y}^C_{UU} - \eta_c}{1 + \eta_c - \eta_c\,\mathcal{Y}^C_{UU}} \tag{36}$$

with

$$\eta_c = C_{\Delta\Omega} - C_\epsilon - 2C_\epsilon C_{\Delta\Omega}\,. \tag{37}$$

Assuming an eventual range of efficiency and solid angle corrections, the magnitude of the corrections to raw unpolarized YCA can be determined as the deviation of A^C_{UU}, given by Eq. 36, with respect to $\mathcal{Y}^C_{UU}$. The left panel of Fig. 18 reports the envelope of the possible corrections assuming C_ϵ and $C_{\Delta\Omega}$ values within ± 0.05 (or ± 0.02), corresponding to a 10% (4%) relative change between electron and positron data taking. These corrections can be sizeable but are exactly calculable once efficiency and solid angle effects are known.

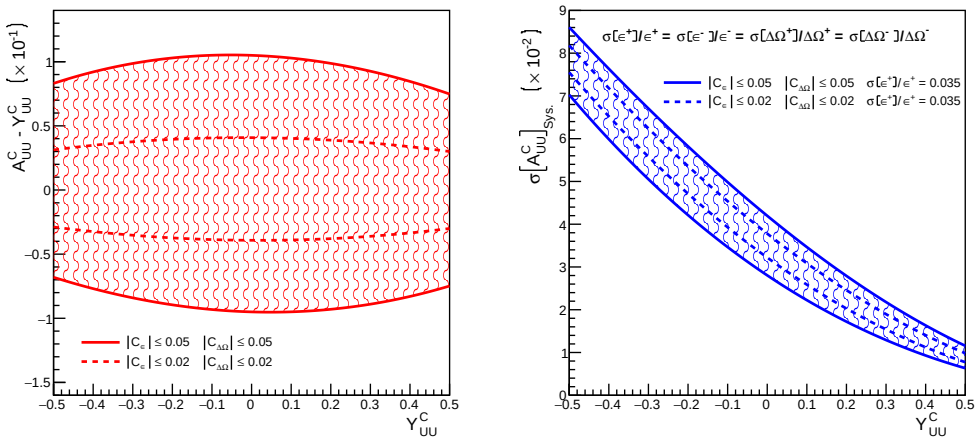

Figure 18. Amplitude of the corrections of unpolarized raw asymmetries (left) and of the corresponding systematic error on unpolarized BCA (right). The shaded areas indicate the possible values of the corrections for a fixed raw asymmetry assuming that the efficiency and solid angle corrections are comprised within ±5% (solid line) and ±2% (dashed line). Asymmetry systematics is evaluated assuming 3.5% relative uncertainty on efficiency and solid angles.

The precision on these corrections directly enters the systematic error on the unpolarized BCA, which can be defined as

$$\sigma\left[A^C_{UU}\right]_{Sys.} = \sqrt{\left(\frac{dA^C_{UU}}{dC_\epsilon}\,\sigma\left[C_\epsilon\right]\right)^2 + \left(\frac{dA^C_{UU}}{dC_{\Delta\Omega}}\,\sigma\left[C_{\Delta\Omega}\right]\right)^2}\,. \tag{38}$$

The right panel of Fig. 18 reports, within the same conditions than the left panel, the envelope of systematic errors related to efficiency and solid angle corrections assuming a 3.5% relative accuracy on $\epsilon^\pm$ and $\Delta\Omega^\pm$. These correspond to a total 5% relative systematic uncertainty of the cross section. Under these assumptions, the absolute systematic uncertainties on unpolarized BCA are contained within 0.01-0.09 depending on the magnitude of $\mathcal{Y}^C_{UU}$.

Similarly, the polarized YCA is written

$$\mathcal{Y}^C_{LU} = \frac{(Y^+_+ - Y^+_-) - (Y^-_+ - Y^-_-)}{Y^+_+ + Y^+_- + Y^-_+ + Y^-_-} \tag{39}$$

from which the true polarized BCA, considering efficiency and solid angle corrections, is obtained as

$$A^C_{LU} = \left[1 + \eta_c\left(1 + A^C_{UU}\right)\right]\,\mathcal{Y}^C_{LU} - \eta_c\left(1 + A^C_{UU}\right)A^+_{LU}\,. \tag{40}$$

The magnitude of efficiency and solid angle corrections effects and related absolute systematic uncertainties for polarized BCA is determined using the same approach as in the upolarized case. According to Eq. 40, these are depending in addition on the positron BSA which is assumed to vary within ±50% (red curves) or ±25% (black curves). The absolute systematic uncertainty related to differences between electron and positron measurements may

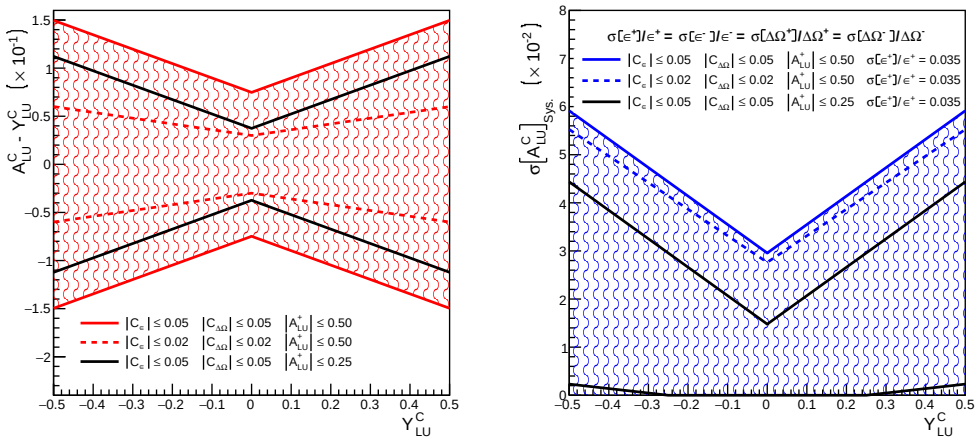

Figure 19. Amplitude of the corrections of polarized raw asymmetries (left) and of the corresponding systematic error on polarized BCA (right). The shaded areas indicate the possible values of the corrections for a fixed raw asymmetry assuming that the positron BSA is comprised within ±50%, and that the efficiency and solid angle corrections take values within ±5% (solid line) and ±2% (dashed line). The solid black line limits the variation domain when the positron BSA is comprised within ±25%. Asymmetry systematics is evaluated assuming a 3.5% relative uncertainty on efficiency and solid angles.

amount up to 0.06 in the case of large asymmetries.

Finally, the true neutral BSA is expressed

$$A^0_{LU} = \left[1 + \eta_c \left(1 + A^C_{UU}\right)\right] \mathcal{Y}^0_{LU} - \eta_c \left(1 + A^C_{UU}\right) A^+_{LU} \tag{41}$$

where

$$\mathcal{Y}^0_{LU} = \frac{(Y^+_+ - Y^+_-) + (Y^-_+ - Y^-_-)}{Y^+_+ + Y^+_- + Y^-_+ + Y^-_-} \tag{42}$$

is the neutral yield spin asymmetry. The determination of the magnitude of the corrections of raw asymmetries and their attached systematics reported on Fig. 19 is also valid for the neutral BSA. In the twist-2 approximation where the neutral BSA is predicted to be zero, systematics effects may account for up to 0.03 depending essentially on the magnitude of the positron BSA.

The effect of eventual efficiency and solid angle dissymmetries between electron and positron data taking can generally be sizeable but can be corrected for with high accuracy by calibrating simulations with specific measurements of a knwon physics process. In this context, the 3% relative uncertainty assumption should be considered as a maximal value.

7 Beam time request

For the main physics program we request 80 days of 5-pass secondary electron and positron beams at an energy of 10.6 GeV, and a beam current of

45 nA impinging on a 5 cm long liquid hydrogen target. The beam must be longitudinally polarized with a polarization of λ=60% or higher. The beam polarization must be switched at a rate of 30 Hz with direct reporting, and the charge asymmetry between each helicity state must be kept below 0.1%. These figures are supplemented with 8 days of background calibration studies. In addition, we request 6 days of 1-pass electron beam at the same current of 40 nA for systematic effects and cross calibration purposes of the beam line instrumentation, and 6 days of commissionning of the Hall B equipment with the positron beam.

7.1 Proposed measurements

Purpose	Label	Beam parameters					Target	Sol. Pol.	Tor. Pol.	Time (h)
		q (e)	Nat.	E (GeV)	I (nA)	λ (%)				
$ep \to ep$	Cal.	−	P	2.2	45	0	5 cm LH_2	−	+	24
								+		24
			S					+		24
								−		24
$ep \to ep\gamma$	Phy.			10.6		60		−		480
Background	Cal.							−		48
$ep \to ep\gamma$	Phy.							+		480
Background	Cal.							+		48
Commissioning		+	S	2.2	45	0	5 cm LH_2	+	−	72
$ep \to ep$	Cal.							+		24
								−		24
Commissioning				10.6		60		−		72
$ep \to ep\gamma$	Phy.							−		480
Background	Cal.							−		48
$ep \to ep\gamma$	Phy.							+		480
Background	Cal.							+		48
								Total		**2400**

Table 2. Detailed description of the beam time request. The beam nature label P indicates the CEBAF primary electron beam, and S indicates the secondary electron or positron beam generated at the positron production target. The data taking label Cal. stands for calibration, and Phy. for physics data taking.

The measurements of this proposal are detailed in Tab. 2, and comprise physics data taking with both electron and positron beams. Electron data using the secondary electron beam generated at the positron production target will be used to compare with positron data for constructing BCA observables. From the statistics and systematics point of views, a direct comparison with RGA

data would provide degraded BCA observables. Indeed, RGA operated with several experimental configurations such that the positron-like configuration (Torus in out-bending mode and FTCal on) represents in the best case 25% of accumulated data, *i.e.* about a factor 2 less statistics than the expected positron statistics. Furthermore, positron beam properties are expected to be different from the CEBAF electron beam properties. The larger beam emittance motivates the use of a new target cell with diameter larger than RGA target cell, such that systematics attached to the target would not compensate in a comparison with RGA data. The previous section (Sec. 6) reviews the systematic effects attached to `CLAS12` operation in positron mode and motivates data taking with different solenoid polarities, a further variation with respect to RGA configuration. Comparing electron and positron data taken with similar statistics, the same beam properties, the same target cell, the same detector status, and the same detector configuration is the path we are proposing to miminize systematic effects and provide high quality BCA observables.

Immediately before the beginning of the physics run, short electron beam runs will be performed to enable checking for false charge asymmetries by employing elastic $e^-p \to e^-p$ scattering with a 1-pass beam. This comprises using both the primary CEBAF electron beam and the secondary beam generated at the positron production target, together with negative and positive solenoid polarities. The electron beam physics run will be conducted over a period of 40 days, alternating solenoid polarities and using the secondary electron beam produced simultaneously with the positron beam at the production target of the positron source.

After the polarity change of CEBAF, the Hall B beamline equipment and polarimeter will be commissioned with the positron beam at 1-pass, and a short run on the $e^+p \to e^+p$ elastic scattering will be performed for direct comparison with electron calibration data. For this comparison elastic kinematics at low Q^2 will be selected to limit the 2-photon contributions to less than 2-3%. After commissioning Hall B equipment with a 5-pass positron beam, the $e^+p \to e^+p\gamma$ DVCS physics run will be conducted.

Polarization measurements will be carried out regularly every 2-3 days initially, and once a week during stable running periods. The current plan is to use Bhabha scattering on a polarized ferromagnetic foil (see Appendix A). Asymmetries are measured by flipping the positron beam polarization and detecting the scattered electrons and positrons in coincidence. The asymmetry is same magnitude as for polarized electron beams.

Additional calibration runs will also be conducted all along the physics run for detector calibration and background studies. Production data taking is expected with a trigger rate of up to 20 KHz and a data rate of up to 800 MB/s. Once a week during stable operation, luminosity scan will be carried out and randomly triggered data will be taken at various beam currents to simulate realistic background conditions to be used for Monte Carlo simulations.

The total beam time request amounts to 2400 hours (100 days) of data taking.

7.2 Experimental projections

Expected experimental data are shown in Fig. 20-25 at small and intermediate t using the BM modeling of DVCS observables [Bel10] and the KM CFF [Kum10], for the binning used in Sec. 3 to evaluate the impact of positron measurements on the CFF extraction. Statistical error bars assume 80 days DVCS data taking equaly shared between secondary electron and positron beams. The data represented in these figures correspond to a selected set of the data that will be obtained. Typical ϕ-distributions of A_{UU}^{C} (Fig. 20-21), A_{LU}^{C} (Fig. 22-23), and A_{LU}^{+} (Fig. 24-25) are shown for different (x_B, Q^2)-bins. The (x_B, Q^2, t) sensitivity of the magnitude and shape of A_{UU}^{C} is particularly noticed. In general, the accuracy of expected data will allow us to identify and quantitify the ϕ-modulation of DVCS observables with a precision which decreases as (x_B, Q^2) increase.

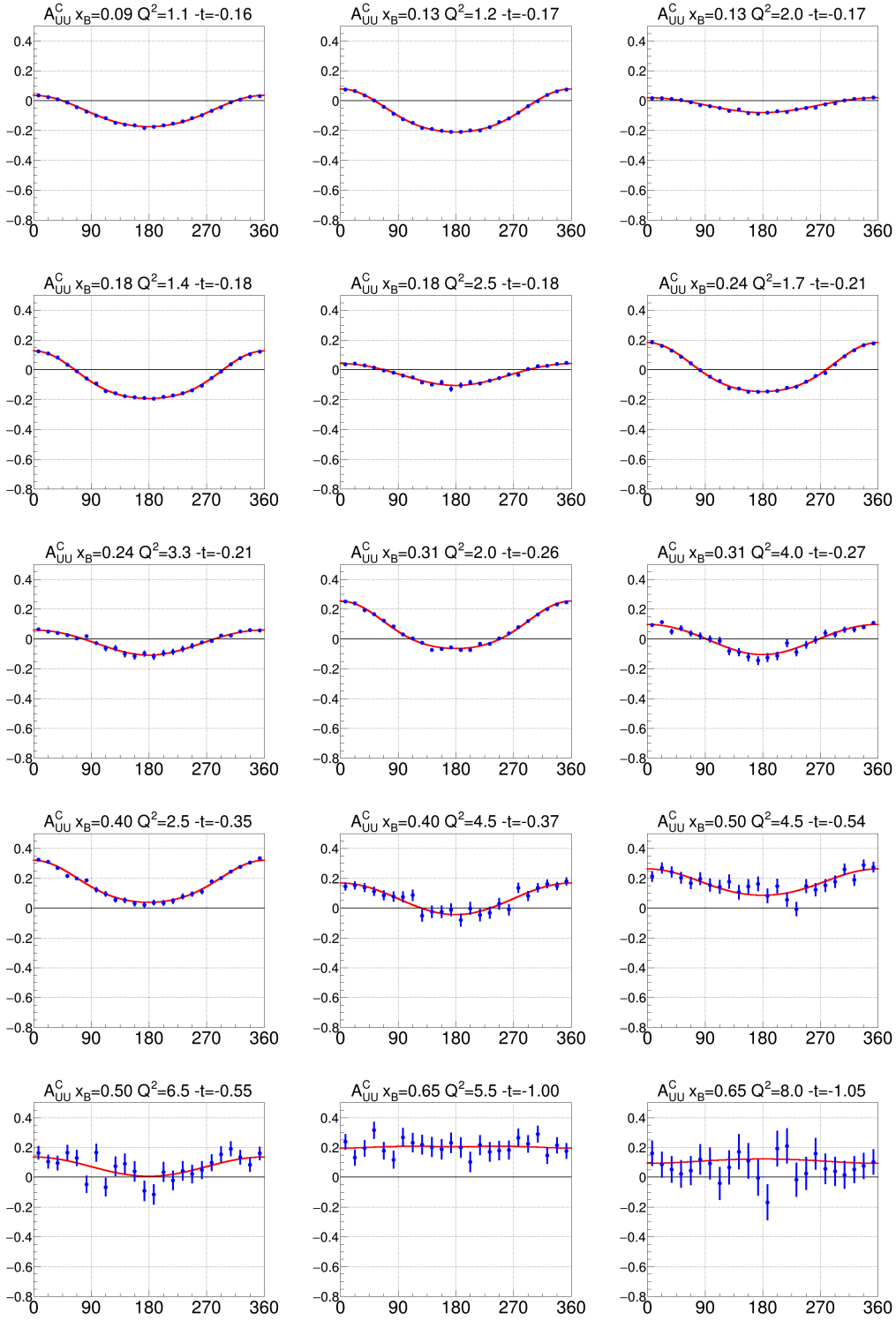

Figure 20. Projected A^C_{UU} data in selected small t-bins at a 10.6 GeV positron and electron beam energy.

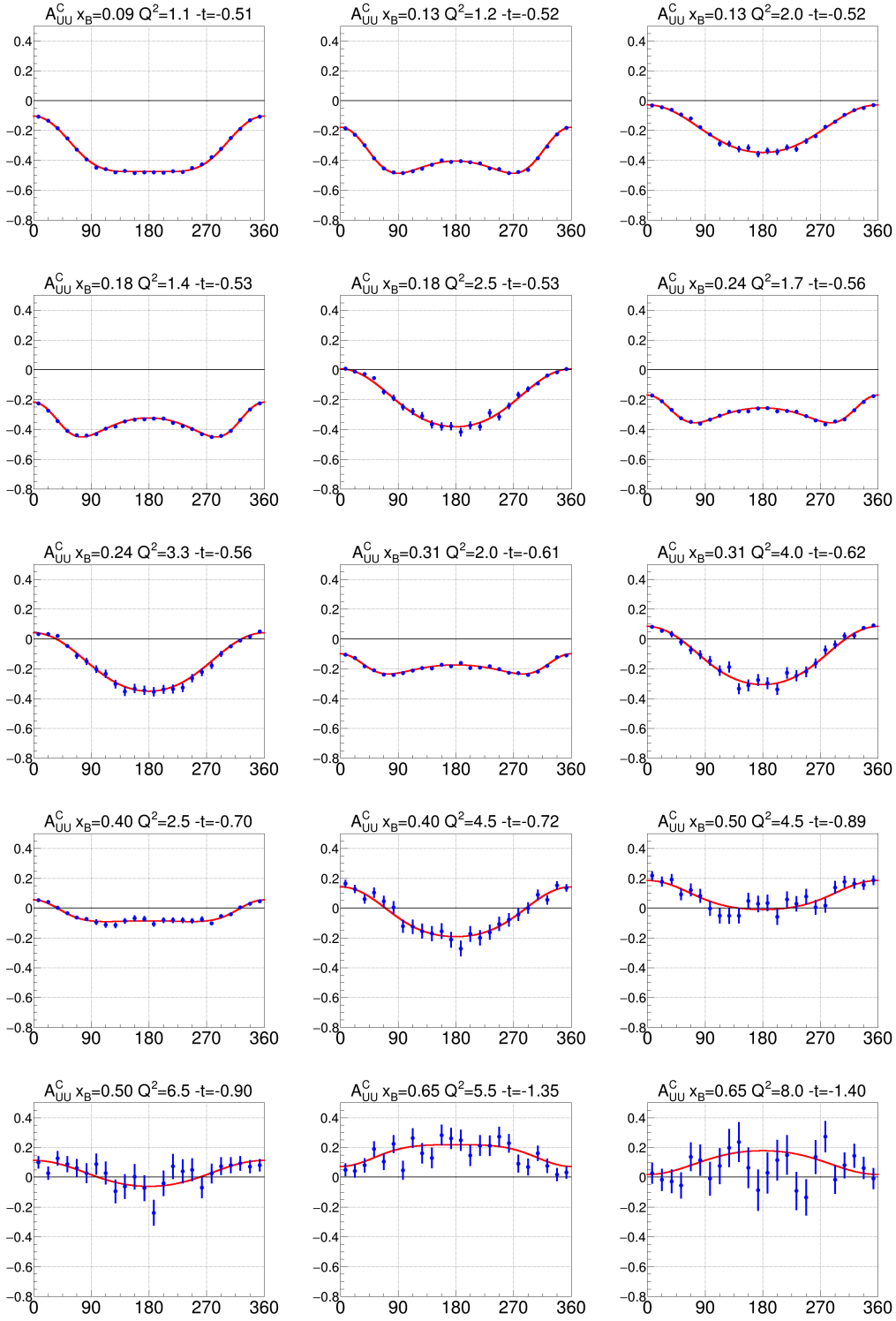

Figure 21. Projected A^C_{UU} data in selected intermediate t-bins at a 10.6 GeV positron and electron beam energy.

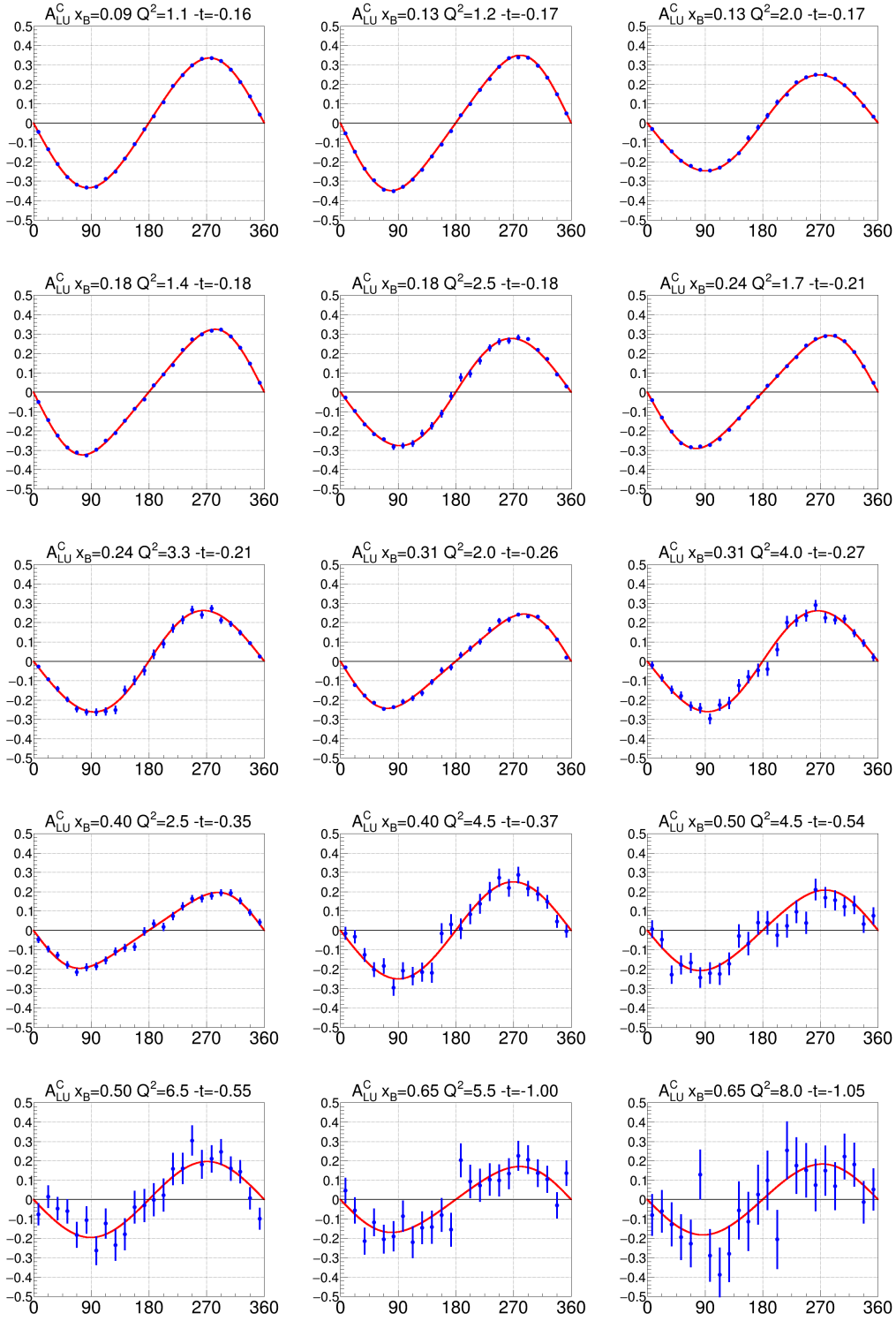

Figure 22. Projected A_{LU}^{C} data in selected small t-bins at a 10.6 GeV positron and electron beam energy.

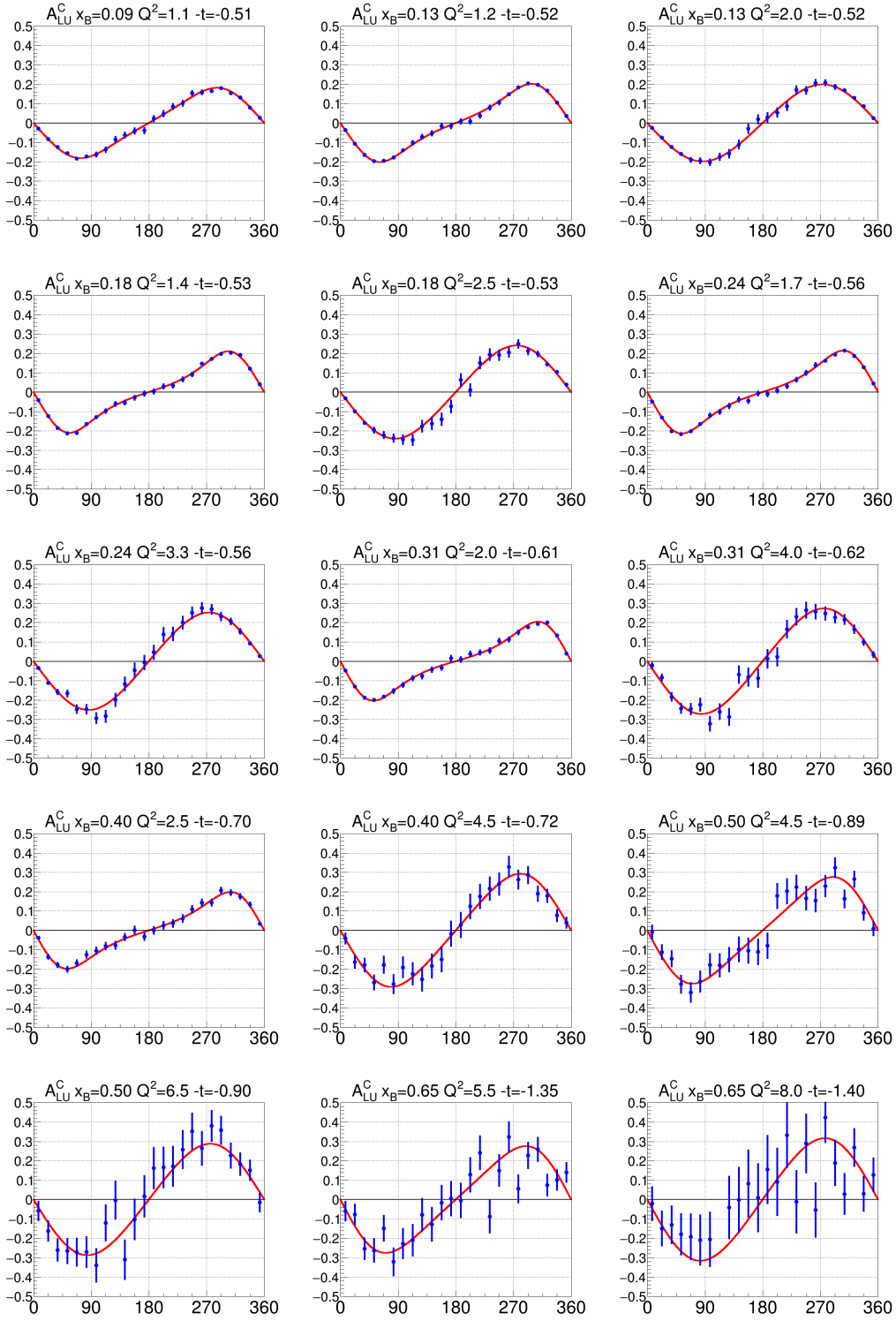

Figure 23. Projected A^C_{LU} data in selected intermediate t-bins at a 10.6 GeV positron and electron beam energy.

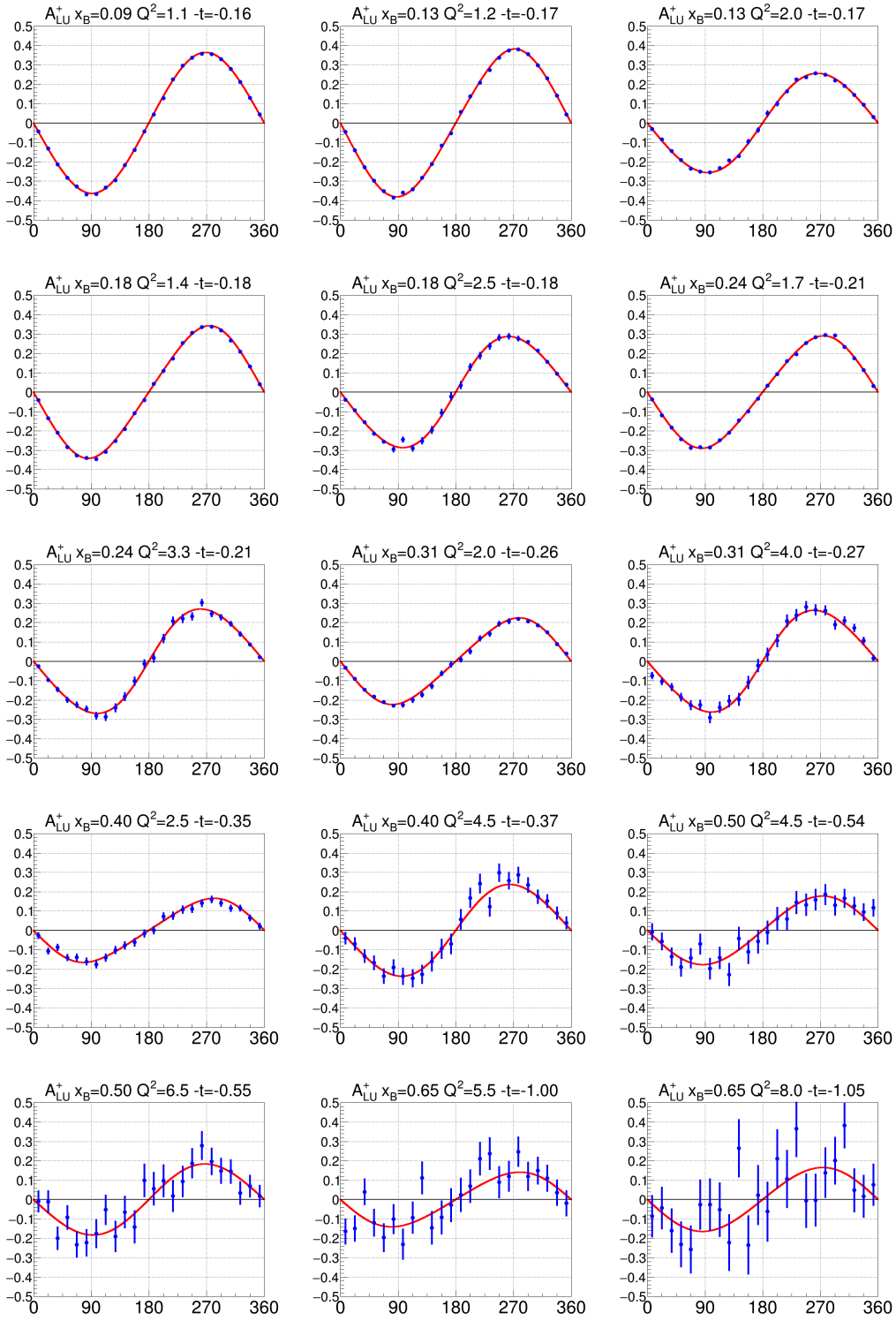

Figure 24. Projected A^+_{LU} data in selected small t-bins at a 10.6 GeV positron beam energy.

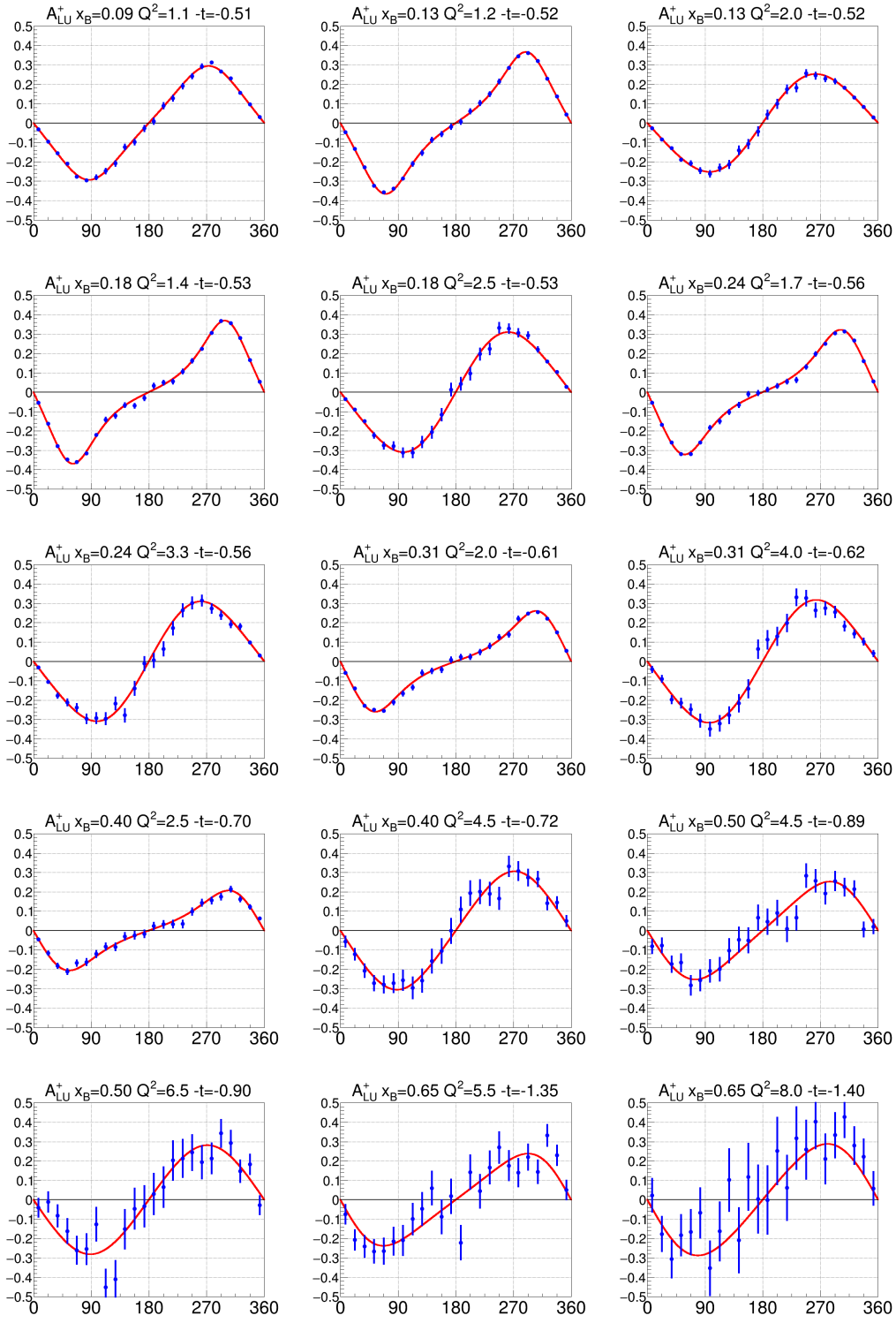

Figure 25. Projected A^+_{LU} data in selected intermediate t-bins at a 10.6 GeV positron beam energy.

A Beam polarization measurement

The positron beam polarization can be measured using Bhabha scattering, where an incident positron scatters off an electron in a polarized metallic target. The most likely option for the design of a Bhabha polarimeter is to modify the existing Møller polarimeter to accommodate positrons. Though the cross section for Bhabha and Møller scattering are different, the analyzing power (A_{zz}) for a longitudinally polarized beam and a longitudinally polarized target are the same [Ale02]

$$A_{zz}\left(\theta_{CM}\right) = -\frac{\left(7+\cos\theta_{CM}\right)\sin^2\theta_{CM}}{\left(3+\cos^2\theta_{CM}\right)^2} \tag{A.1}$$

where θ_{CM} is the center of momentum scattering angle. Particularly, A_{zz} has a maximum magnitude of 7/9 at $\theta_{CM} = 90°$, which is the central scattering angle of the existing Møller polarimeter. Forming the beam-helicity-dependent asymmetry gives

$$\mathcal{A} = \left(\frac{d\sigma^+}{d\Omega} - \frac{d\sigma_-}{d\Omega}\right) \Big/ \left(\frac{d\sigma^+}{d\Omega} + \frac{d\sigma_-}{d\Omega}\right) = A_{zz}\left(\theta_{CM}\right)\, P_B^z P_T^z, \tag{A.2}$$

where the $\pm$ refers to cases where the beam polarization (P_B^z) and the target polarization (P_T^z) are aligned or anti-aligned. The asymmetry is measured from the yields according to

$$\mathcal{A} = \frac{N_+ - N_-}{N_+ + N_-} = \langle A_{zz}\rangle\, P_B^z P_T^z\,, \tag{A.3}$$

where $\langle A_{zz}\rangle$ is the effective analyzing power corrected for the finite-angle acceptance of the polarimeter and atomic-electron motion (also known as the Levchuk effect [Lev94]). The CLAS12 Møller polarimeter detects the scattered electrons in coincidence near $\theta_{CM} = 90°$, the peak of A_{zz}. As compared to single-arm Møller polarimetry, the coincidence method has the advantage of producing a clean data set without having to do energy-dependent background subtractions (see, for example Ref. [Arr92]). Accidental background rates are typically less than 10% of the real coincident rate at the CLAS12 polarimeter, and is further measured and included as a correction.

The CLAS12 polarimeter, which schematic layout is shown on Fig. A.1, relies upon a pair of quadrupole magnets to separate the scattered electrons from the beam and to deflect the scattered electrons into the detectors. To adapt the CLAS12 Møller polarimeter, the plan is to rewire the quadrupole magnets to act as dipole magnets as shown in Fig. A.2. In this configuration if the electron is scattered to the left and the positron to the right (left figure), the two leptons are bent away from the beamline to the detectors. However, if the positron is scattered to the left and the electron to the right (right figure) both particles will initially be bent toward the beamline and will miss the detectors. This unavoidably results in only half of the leptons scattered at $\theta_{CM} = 90°$ to reach the detectors, thus necessitating longer runs than are presently being

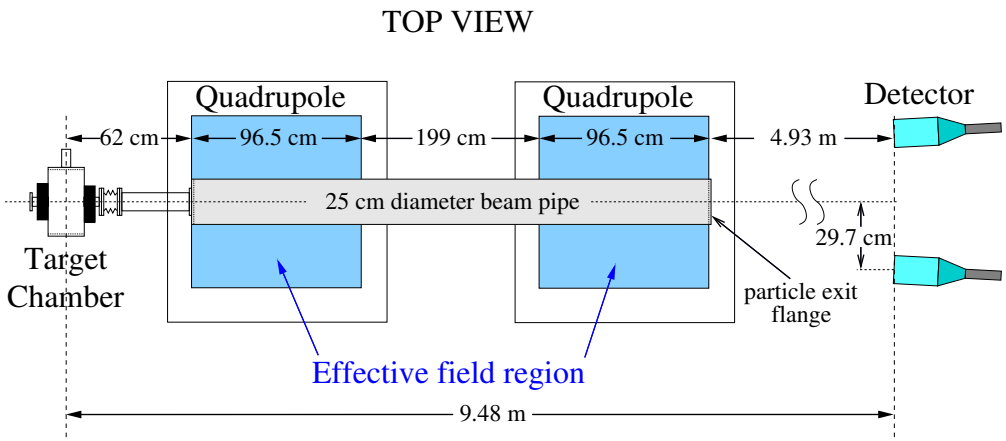

Figure A.1. Layout of the CLAS12 Møller polarimeter; detector shielding is not shown.

done with an electron beam. It will also potentially lead to some increase in accidental background. This can and will be simulated once a full calculation of the magnetic field map is completed. A calculation of the field map has recently been started by the JLab magnet group and should be available so that the simulation can be done prior to submission of this proposal to the PAC. Preliminary calculations show that there will be a residual dipole field along the axis of the magnets, which will result in a deflection of the positron beam. One solution to this is to use corrector magnets downstream of the polarimeter to realign the positron beam onto the beam dump. In case the field along the axis is large, it is possible the beam will be deflected too far for the corrector magnets to be properly realigned onto the dump. A solution to this is to build an alternative beam dump. Once the field maps become available the trajectory of the beam can be included in the simulation and the most appropriate solution can be identified.

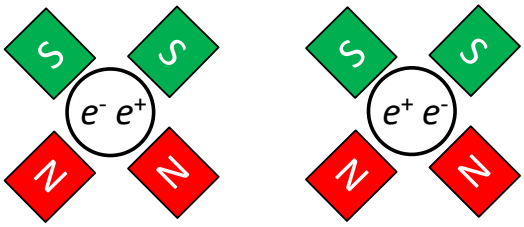

Figure A.2. Møller quadrupoles rewired into a dipole configuration as seen looking along the beam direction. The left (right) panel has electrons (positrons) scattered to the left with positrons (electrons) scattered to the right.

Another concern is the mechanical stresses on the quadrupoles run in dipole mode. The initial expectation of the JLab magnet group is that this is not likely to be a problem but this will have to be verified with a finite-element analysis.

Full simulations for a Bhabha polarimeter will have to be run to optimize the magnetic fields and the locations of detectors and shielding. In the event that it is not possible to run the quadrupoles as dipoles other solutions for positron polarimetry will be explored:

- *Single mode* - Use the present wiring of the quadrupoles and run in singles mode; the expected background in this run-mode is higher than in coincidence mode so simulations have to be performed to understand the effect of the background on measurement times;
- *Coincidence mode* - Use the present wiring and reconfigure detector and shielding locations to identify a coincidence run-mode.

While all these different possibilities will be thoroughly investigated, the *single mode* or *coincidence mode* have the advantage of operating for both electrons and positrons with only changing the magnet current polarity, an important feature for minimizing systematics of polarized BCA measurements. Beyond simulations, the experimental investigation of the *single mode* operation with the CEBAF electron beam may readily provide some answer about the feasibility of this option.

B Polarized positron beams at Jefferson Lab

This appendix is based on current investigations of the impact of positron beam operation at CEBAF, that were collected in the document *Some practical considerations for a positron source and positron beam operations at CEBAF* from P. Degtiarenko, J. Grames, J. Kowal, J. Musson, S. Philip, M. Tiefenbak, and K. Welch [Deg20].

B.1 Radiological considerations

Two potential approaches of producing positron beams are considered: one being a separate new enclosure, the other being the existing injector segment to house the positron source. At the very high level, the first option would be the *safest* from a radiological standpoint, as it would allow shielding to be applied as part of the initial facility design, and allow the shielding and other radiological controls to be optimized as integral part of the design.

At energies above the photo-neutron production threshold (∼10-15 MeV), any design will have to address the shielding of neutrons and photons, plus the activation of materials. A 100 kW-100 MeV system would involve significant shielding, and very high levels of activation in the targets and surrounding materials, plus significant activation of cooling water used in and around the targets, and air activation in the vault. Maintenance would also become a significant issue. The activation would produce a radiological *footprint* similar to one of the beam dumps in Hall A or C. In other words, the positron production facility would in effect create a new *radiological facility* analogous to the Hall A dump, including cooling water systems, and would benefit the most from being separated from the existing beam enclosure.

B.2 Beam power considerations

Considering a positron source based on a 100 kW electron beam power, a reasonable way to produce and capture positrons should be a two-stage design. This would allow to separate the functions of main energy dissipation, and the positron production. The first stage (a radiator and a subsequent beam dump) would absorb the main beam energy, and the positron production stage would see only a few percent of it. This separation would further provides more comfortable heat and radiation conditions for the positron capture hardware. The design choices may also include magnetic field removal of the electron beam, as in the current version of the Compact Photon Source [Day20].

B.3 Personnel and machine protection

From the Personnel Safety System (PSS) perspective, electrical hazard, PSS and ODH controls are hereafter considered:

Electrical hazard - concerning the polarity reversal of the dipoles transporting the beam to experimental halls, the current transducers providing feedback to BELLs system would need to be replaced if installed after the polarity switch;
PSS controls - building a separate positron injector will require to treat it as a separate segment, where all necessary PSS controls would have to be installed, in essence a duplication of the existing injector;
ODH controls - building a separate segment with equipment using significant quantity of cryogens may require installation of an Oxygen Defiency Hazard system.
From the Machine Protection System perspective, there would be in general no need to alter the existing equipment around the site, except the new positron injector area.

B.4 Reversal of CEBAF magnetic field

A tentative list of the electrical systems requiring attention for positron beam delivery is:

1) Trims magnet (∼1900 units);
2) ARC1 to ARC10 (10 units);
3) RSEP8 and RSEP9 (2 units), recirculating septa in the West and East ARC;
4) Dogleg1 to Dogleg9 (9 units);
5) XSEP2, 4, 6, 8, 10 (5 units) extraction region magnets for each of 5 passes;
6) YA 2, 4, 6, 8, 10 (5 units) extraction region thin septa for each of 5 passes;
7) Hall A, B, C, D (5 units) magnets that transport beam into each Hall;
8) BSY Dump (1 unit) which allows beam steered into the dump before Halls A, B, C;
9) Hall A and Hall C Lambertson (2 units);
10) Recirculation and transport shunt modules (109 units);
11) End station A Møller quadrupoles (4 units);
12) End station A Møller and Compton dipoles (2 units);
13) End station C quadrupole magnets (2 units);
14) End station C Compton dipole (1 unit);
15) End station D Tagger magnte (1 unit).

All correctors and quadrupole magnets (except one in Hall C) are bipolar power supplies able to drive positive or negative amperage, and can be used for electron/positron beam without any changes in hardware. Other trim magnets used for position modulation and Fast Feedback are not expected to be affected by the beam charge. All of the bending dipole magnets in CEBAF proper are powered by uni-polar power supplies without polarity reversal switches. Most of the ARC magnets are in a series configuration, meaning that the reversal of the power leads at the supply effectively reverses the field in all of the magnets powered by the individual power supply (see Fig. B.1 for a typical example). Similarly to the power supplies, the shunt modules will also need to have leads reversed on the termination in the upstairs chassis. To reduce the number of reversing operations and to prevent failures/errors, the polarity reversal would have to be an engineered solution. The system would have remotely controlled

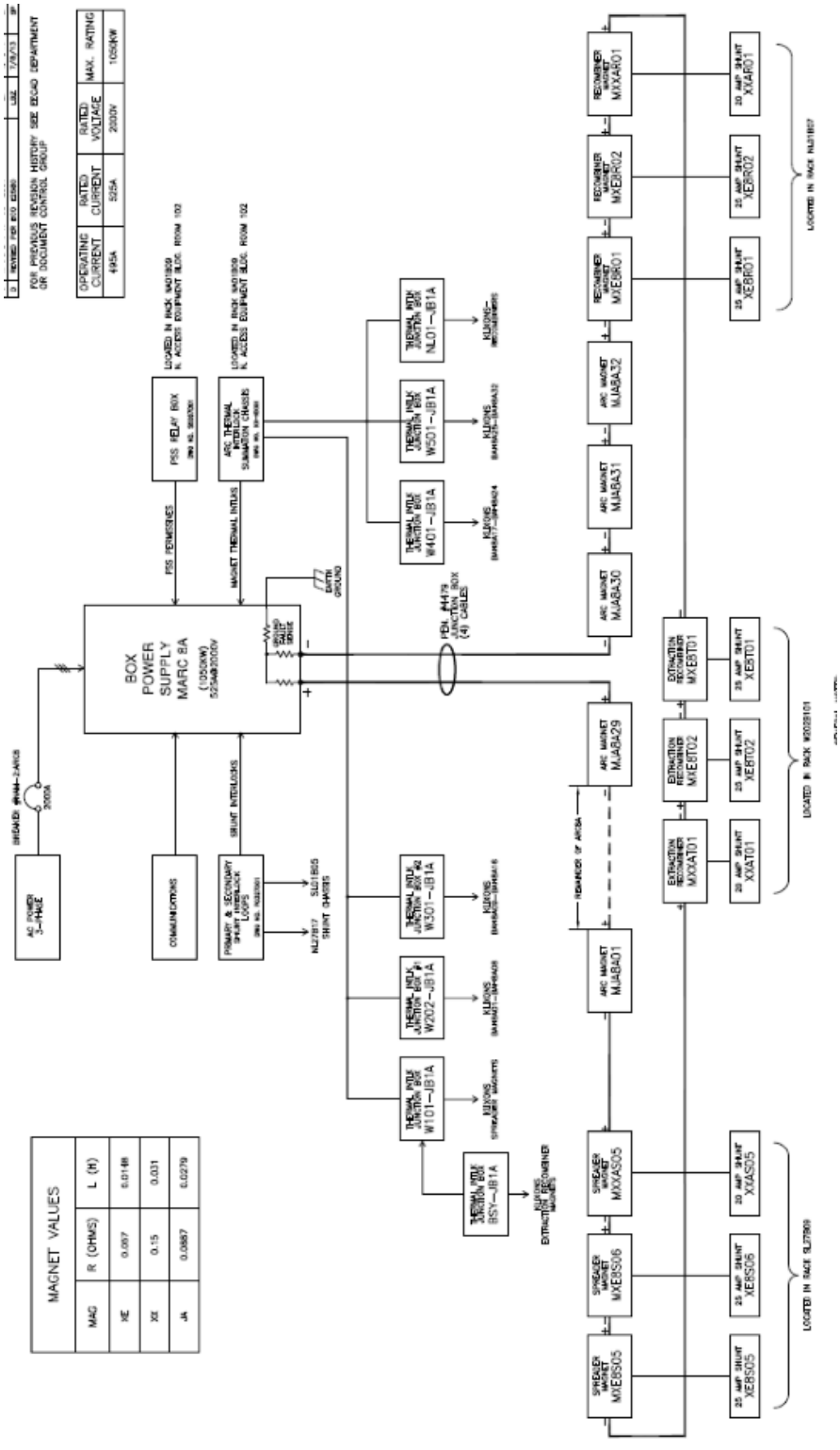

Figure B.1. Typical box power supply for ARC magnets.

switches that can be configured into the correct state for electron or positron beam. Operational procedures would remain unchanged, as the magnet systems are blind to polarity of connection. However, any portion of the accelerator used to create the electron beam for the production of positrons as well as to transport positrons would require special attention procedurally.
Each of the physics halls have normal and superconducting magnets of various kinds that are not controlled by DC power. Their configuration needs should be examined by the various Halls. Additionally, Hall D is using a permanent dipole to prevent beam into the Hall in case of failure of the Tagger magnet. This may need to be rotated to get the same effect.

The various magnets of the accelerator are a mix of bipolar and unipolar configurations. For the bipolar magnets, observations of the relationship between the $\vec{B}\cdot\vec{dl}$ and the current are consistent with no change in magnetic field versus current after unipolar operation. The meter-scale dipole magnets configured as unipolar systems exhibit a remnant field in the 10-15 Gauss range. The most stringent empirical test of the non-influence of this field is the observation of the fine reproducibility of the beam trajectory after dipole string power supply trips to zero current. The uncontrolled magnetic field of the dipoles, involving prospectively a flux reversal as the dipole field collapses, has not been seen to alter the beam trajectory after the multiple hysteresis cycles executed by protocol after such an event. The known observations seem to indicate that the magnet iron is magnetically soft enough at the fields in use in the CEBAF accelerator as to result in no persistent calibration shifts after field reversal and restoration.

B.5 CEBAF diagnostics for positron beams

Since previous positron efforts [Val16, Bergo] have successfully employed DCT, cavity, and button-electrode-based BPM systems, it is our opinion that design for positron production can proceed, based on data obtained from the JLab experience. Following is a summary of diagnostics behavior and metrics.

BCM resolution analysis

Since electrons and positrons differ only by charge (and magnetic moment), polarity is an obvious difference in the electronic signals. Signal polarity is of little significance, since beam current is the result of a magnitude-only measurement of the high-Q cavitiy, which is phase-independent. Also, positron mass and beam size should result in identical beam loading, thereby producing the same cavity response for a given beam current.

JLab is operating since 25 years 33 BCM pillbox cavities employed to provide detailed current information, time of flight measurements, and also as time-of-arrival sensors. Parametric simulation for various expected beam currents has been performed, which agrees with actual beam-based measurements (to within 2 dB). Therefore, it is useful to rely on several rules of thumb, for which receiver electronics can be evaluated in the lab. Using this data, a nomograph

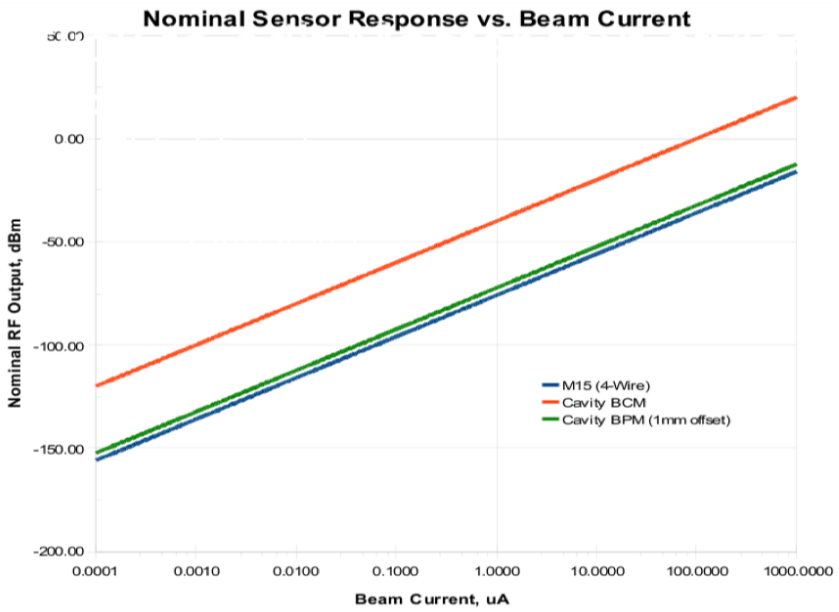

Figure B.2. Nomograph of expected BCM cavity power output (red) for various electron/positron beam currents. Recalling that I_{beam}=1 μA results in -40 dBm of output power, then scaling simply follows $20\log(I_{beam})$.

is produced, which accurately predicts the RF output power (in dBm) for a large range of beam currents. Figure B.2 is a composite of several JLab beamline elements, of which the BCM cavity is shown in red. Knowing the sensor output allows one to quickly establish a linearity constant for I_{beam} versus V_{out}, wich in the case of the standard SS304 JLab BCM cavity is K=447^{-6} μA/μV, for electron and presumably positron beams. For determination of resolution, noise power must be known so as to establish the confidence of the measurement from the resulting signal-to-noise ratio (SNR). If a perfect system is assumed, and sitting in-situ at room temperature (290 K), the noise power for the 50 Ω receiver possessing a 1 Hz bandwidth is calculated from

$$P_n = k_B T B = -174\,\mathrm{dBm} - \mathrm{Hz} \tag{B.1}$$

where k_B is the Boltzmann's constant, T=290 K, and B is the bandwidth. Finally, the resolution of the BCM is

$$\sigma = \delta I_{beam} = \frac{\delta V_{noise}}{K} \approx 1\,\mathrm{pA}\,. \tag{B.2}$$

In reality, cable losses, receiver noise figure, finite bit resolution and the fact that the receivers are intentionally wound for the larger signals of CEBAF impact the ultimate sensitivity. The JLab experience contains solid data for a minimum detectable signal of $\leq$ 500 pA implying a composite noise figure of 27 dB. Much improvement is expected with the JLab digital diagnostics recievers which posess a 4 dB noise figure.

BPM analysis

Low-Q BPM sensors are somewhat problematic, since they often rely on a directional characteristic. The M15 BPM at CEBAF are open-wire, 200 Ω structures which, when used with the standard 50 Ω receiver, have moderate directivity, but are not fully reliant on that quality. It was shown [Bar91] that, regardless of how the BPM is installed, usable signal is available. With respect to electronics, BPM detection is a relative measurement (aside from any 4-wire applications). Therefore, as long as the change in response is common to all four sensor electrodes (antennas), then a calculated position should be available. It is likely that, for any units which have had field mapping and bench calibrations, the relationship between electrical and physical centers would be altered. Reversing the necessary BPM sensors within the beamline is an obvious solution if it appears that sensitivity or orthogonality is compromised.

Assuming nearly-identical behavior for electron and positron beams, the BPM resolution follows as before, by establishing a sensor output, calculating expected noise voltage (V_n), and applying to the position calculation algorithm. Here, however, the algorithm may have several forms, which affects the sensitivity a given SNR has on the result. For one-dimension, the resolution writes

$$\sigma_X = \frac{a}{2\sqrt{2}} \frac{1}{\sqrt{SNR}} = \frac{a}{2\sqrt{2}} \frac{V_n}{V_s} \tag{B.3}$$

where V_s is the signal voltage. Considering the JLab M15 BPM, the typical output power for 100 nA is -102 dBm. Expected noise power for a receiver having a 10 dB noise figure and 10 Hz bandwidth is -154 dBm. So, the resulting 52 dB SNR predicts a resolution of 10 μm. Note that the resolution scales inversely with current, and as the square-root of bandwidth. So, at 10 nA, 1 Hz, the expected resolution becomes 30 μm. Table B.1 provides the performance of BCM and BPM in use at JLab.

I_{beam} (μA)	BCM (dBm)	σ_{BCM} @ 1 Hz (pA)	BPM (dBm)	σ_{BPM} @ 1 Hz (μm)
0.01	-80	≤ 500	-120	30
0.10	-60		-100	3
1	-40		-80	0.3
10	-20		-60	0.03
100	0		-40	0.003

Table B.1. Summary of expected BCM and M15 BPM performance from JLab experience.

References

[Aar09] (H1 Collaboration) F.D. Aaron *et al.* Phys. Lett. B **681** (2009) 391.

[Abb16] (PEPPo Collaboration) D. Abbott *et al.* Phys. Rev. Lett. **116** (2016) 214801.

[Add10] P. Adderley *et al.* Phys. Rev. Acc. Beams **13** (2010) 010101.

[Afa17] A. Afanasev, P.G. Blunden, D. Hasell, B.A. Raue, Prog. Part. Nucl. Phys. **95** (2017) 245.

[Air08] (HERMES Collaboration) A. Airapetian *et al.* J. High Energ. Phys. **06** (2008) 066.

[Air09] (HERMES Collaboration) A. Airapetian *et al.* J. High Energ. Phys. **11** (2009) 083.

[Air12] (HERMES Collaboration) A. Airapetian *et al.* J. High Energ. Phys. **07** (2012) 032.

[Akh19] (COMPASS Collaboartion) R. Akhunzyanov *et al.* Phys. Lett. B **793** (2019) 188.

[Ale02] G. Alexander, I. Cohen, Nucl. Inst. Meth. A **486** (2002) 552.

[Ale08] G. Alexander *et al.* Phys. Rev. Lett. **100** (2008) 210801.

[Ani07] I.V. Anikin, O.V. Teryaev, Phys. Rev. D 76 (2007) 056007.

[Arr92] J. Arrington *et al.* Nucl. Inst. Meth. A 311 (21992) 39.

[Asc13] E.C. Aschenauer, S. Fazio, K. Kumerički, D. Müller, J. High Energ. Phys. **09** (2013) 093.

[Ava09] H. Avakian, V. Burkert, V. Guzey, JPos09 AIP Conf. Proc. 1160 (2009) 43.

[Bar91] W. Barry, Nucl. Inst. Meth. A **301** (1991) 407.

[Bel02] A.V. Belitsky, D. Müller, Nucl. Phys. A **711** (2002) 118c.

[Bel02-1] A.V. Belitsky, D. Müller, A. Kirchner, Nucl. Phys. B **629** (2002) 323.

[Bel04] A.V. Belitsky, X. Ji, F. Yuan, Phys. Rev. D **69** (2004) 074014.

[Bel05] A.V. Belitsky, A.V. Radyushkin, Phys. Rep. **418** (2005) 1.

[Bel10] A.V. Belitsky, D. Müller, Phys. Rev. D **82** (2010) 074010.

[Ber18] B. Berthou *et al.* Eur. Phys. J. C **78** (2018) 478.

[Bergo] https://www.bergoz.com/en/mx-bpm

[Bet34] H.A. Bethe, W. Heitler, Proc. Roy. Soc. London A **146** (1934) 83.

[Bur00] M. Burkardt, Phys. Rev. D **62** (2000) 071503.

[Bur07] M. Burkardt, (2007) arXiv:0711.1881.

[Bur18] V. Burkert, L. Elouadrhiri, F.-X. Girod, Nature **557** (2018) 396.

[Bur20] V. Burkert *et al.* Nucl. Inst. Meth. A **959** (2020) 163419.

[Bra14] V.M. Braun, A.N. Manashov, D. Müller, B. Pirnay, Phys. Rev. D **89** (2014) 074022.

[Car18] (PEPPo Collaboration) L. Cardman, JPos17 AIP Conf. Proc. **1970** (2018) 050001.

[Day20] D. Day *et al.* Nucl. Inst. Meth. A **957** (2020) 163429.

[Def17] (Hall A Collaboration) M. Defurne *et al.* Nature Comm. **8** (2017) 1408.

[Deg20] P. Degtiarenko, J. Grames, J. Kowal, J. Musson, S. Philip, M. Tiefenback, K. Welch, Private Communication (2020).

[Die02] M. Diehl, Eur. Phys. J. C **25** (2002) 223.

[Die03] M. Diehl, Phys. Rep. **388** (2003) 41.

[Die07] M. Diehl, D.Y. Ivanov, Eur. Phys. J. C **52** (2007) 919.

[Die09] M. Diehl, *Cont. to the CLAS12 European Workshop*, Genova (Italy), 2009.
[Dum11] J. Dumas, Doctorate Thesis, Université Joseph Fourier, Grenoble, 2011.
[Gol10] S. Golge, Ph.D. Thesis, Old Dominion University, Norfolk (VA, USA), 2010.
[Gra11] J. Grames, E. Voutier *et al.* Jefferson Lab Experiment **E12-11-105** (2012).
[Gra18] (JLab Positron Working Group) J. Grames, E. Voutier *et al.* Jefferson Lab **LOI12-18-004** (2018); arXiv:1906.09419 (2019).
[Gui08] M. Guidal, Eur. Phys. J. A **37** (2008) 319; [Erratum-ibid. A **40** (2009) 119].
[Ji97] X. Ji, Phys. Rev. Lett. **78** (1997) 610.
[Ji03] X. Ji, Phys. Rev. Lett. **91** (2003) 062001.
[Kum08] K. Kumerički, D. Müller, K. Passek-Kumerički, Nucl. Phys. B **794** (2008) 244.
[Kum10] K. Kumerički, D. Müller, Nucl. Phys. B **841** (2010) 1.
[Kum11] K. Kumerički, D. Müller, A. Schäfer, J. High Energ. Phys. **07** (2011) 073.
[Kum16] K. Kumerički, S. Liuti, H. Moutarde, Eur. Phys. J. A **52** (2016) 157.
[Kum19] K. Kumerički, Nature **570** (2019) E1.
[Kur10] E.A. Kuraev, Y. Bystritskiy, M. Shatnev, E. Tomasi-Gustafsson, Phys. Rev. C **81** (2010) 055208.
[Lev94] L.G. Levchuk, Nucl. Inst. Meth. A **345** (1994) 496.
[May51] M.M. May, Phys. Rev. **84** (1951) 265.
[Mec03] (CLAS Collaboration) B. Mecking *et al.* Nucl. Inst. Meth. **503** (2003) 513.
[Mou19] H. Moutarde, P. Sznajder, J. Wagner, Eur. Phys. J. **79** (2019) 614.
[Mul94] D. Müller, D. Robaschick, B. Geyer, F.M. Dittes, J. Hořejši, Fortschr. Phys. **42** (1994) 101.
[Ols59] H. Olsen, L. Maximon, Phys. Rev. **114** (1959) 887.
[Omo06] T. Omori *et al.* Phys. Rev. Lett. **96** (2006) 114801.
[PAC46] https://www.jlab.org/exp_prog/PACpage/PAC46
[Pol99] M.V. Polyakov, C. Weiss, Phys. Rev. D **60** (1999) 114017.
[Pol03] M.V. Polyakov, Phys. Lett. B **555** (2003) 57.
[Pol08] M.V. Polyakov, Phys. Lett. B **659** (2008) 542.
[Pol18] M.V. Polyakov, P. Schweitzer, Int. J. Mod. Phys. A **33** (2018) 1830025.
[Ral02] J.P. Ralston, B. Pire, Phys. Rev. D **66** (2002) 111501.
[Rob17] Y. Roblin, *Cont. to the JPos17 International Workshop on Physics with Positrons at Jefferson Lab*, Newport News (USA, VA), 2017.
[Sok64] A.A. Sokolov, I.M. Ternov, Sov. Phys. Dokl. **8** (1964) 1203.
[Som31] A. Sommerfeld, Ann. Physik **11** (1931) 257.
[Val16] P. Valente *et al.* INFN-16-04/LNF (2016).
[Van99] M. Vanderhaeghen, P.A.M. Guichon, M. Guidal, Phys. Rev. D **60** (1999) 094017.
[Wic51] G.C. Wick, Phys. Rev. **81** (1951) 467.